Structural health monitoring of tendons in a multibody floating offshore wind turbine under varying environmental and operating conditions

Christos S. Sakaris [a], Yang Yang [b], Musa Bashir [a,*], Constantine Michailides [c], Jin Wang [a], John S. Sakellariou [d], Chun Li [e]

[a] *Department of Maritime and Mechanical Engineering, Liverpool John Moores University, Liverpool, Byrom Street, L3 3AF, UK*

[b] *Faculty of Maritime and Transportation, Ningbo University, Ningbo, 315211, P.R. China*

[c] *Department of Civil Engineering and Geomatics, Cyprus University of Technology, 2-8 Saripolou, 3036 Limassol, Cyprus*

[d] *Department of Mechanical Engineering & Aeronautics, University of Patras, GR 26504 Patras, Greece*

[e] *School of Energy and Power Engineering, University of Shanghai for Science and Technology, Shanghai, 200093, P.R. China*

Abstract: The structural health monitoring of a Floating Offshore Wind Turbine (FOWT) tendons, taking into account the comprehensive damage diagnosis problem of damage detection, damaged tendon identification and damage precise quantification under varying environmental and operating conditions (EOCs), is investigated for the first time. The study examines a new concept of a 10 MW multibody FOWT whose tower is supported by a platform consisting of two rigid-body tanks connected by 12 tendons. Normal and the most severe EOCs from a site located in the northern coast of Scotland, are selected for the simulation of the FOWT structure under constant current but varying wind and wave conditions. Dynamic responses of the platform under different damage states are obtained based on the simulated FOWT. The damage scenarios are modelled via stiffness reduction (%) at the tendon's connection point to the platform's upper tank. Damage diagnosis is

* Corresponding author: m.b.bashir@ljmu.ac.uk

achieved via an advanced method, the Functional Model Based Method, that is formulated to operate using a single response signal and stochastic Functional Models representing the structural dynamics under the effects of varying EOCs and any magnitude of the considered damages. Due to the robustness and high number of the existing tendons, the effects of considered damages on the FOWT dynamics are minor and overlapped by the effects of the varying EOCs, indicating a highly challenging damage diagnosis problem. Very good damage detection results are obtained with the damage detection almost faultless and with no false alarms. Accurate tendon identification is achieved for the 95% of the considered test cases, while the mean error in damage quantification is approximately equal to 4% using measurements from just a single accelerometer within a very limited frequency bandwidth of [0-5] Hz.

Keywords: Damaged tendon diagnosis, Structural Health Monitoring, Functional Models, Statistical time series methods, Floating Offshore Wind Turbine, Varying environmental and operating conditions

1. Introduction

Structural Health Monitoring (SHM) of offshore structures such as fixed and floating platforms for Offshore Wind Turbines (OWTs), is vital as damage on critical parts may lead to loss of stability, inefficient operation or total loss of asset. Offshore structures operate under varying Environmental and Operating Conditions (EOCs) such as wind speed (WS), significant wave height (SWH), current, temperature and others, which partially or fully "mask" the effects of damages on the structural dynamics, rendering SHM highly challenging [1-4]. The SHM of tendons [5-8], mooring lines [9-13], offshore platforms [14-21] and OWT towers [21-23], has been mostly investigated albeit under constant EOCs. However, the realistic case of varying EOCs that significantly affects the structural dynamics and makes SHM difficult, has been considered only in a limited number of studies [1-3, 24-25] with focus mostly on platforms and towers of OWTs. More so, these studies were confined only to the first level of SHM, which is damage detection [26].

The damage detection methods employed in the above studies are conducted using a data-based model such as a state space [1, 25] or a regression [2, 24] models. The data-based model is exclusively developed using vibration signals from the healthy structure and measurements of the EOCs. Model features which are sensitive to damage, such as its residual signal and selected modal parameters are acquired for damage detection. Thus, based on the explicit modelling [27, 28] of the varying EOCs' effects on the dynamics of healthy OWTs and measurements of the present EOCs, damage detection is achieved through a comparison of the features of the present (unknown structural state) model with their counterparts from the healthy dynamics. These methods usually require several sensors, multiple vibration signals and continuous measurements of the varying EOCs both in the baseline (method's training) and inspection (diagnostics in real time) phases [1-3, 24-25]. The use of several sensors and EOCs measurements are often costly and impractical.

Recently, a novel approach has been exclusively presented for damage detection under varying EOCs. The main advantage of this approach over the previous methods is that no measurable EOCs are needed in the diagnostics phase [27, 28], leading to reduced cost and equipment. This approach is based on the general framework of the Functional Model Based Method (FMBM) [29], which has been successfully applied for damage detection under varying EOCs in a railway vehicle suspension [27] and a composite beam [28]. In these referenced studies, the healthy structural dynamics under varying EOCs are modelled via a stochastic Functional Model (FM) whose parameters are expressed as functions of the EOCs. Additionally, the FM is based on a concept of representing the transmittance function [30] under varying EOCs using a pair of vibration response signals received via two sensors (one sensor per signal), with one measurement point taken as input and the other as output. A further advantage of this approach is that the FM is estimated using a relatively low number of response signal pairs, while the operating parameter that includes the EOCs may be scalar or vector of any dimension according to the population of the EOCs. Two types of FMs have been used in this FMBM version [27, 28], a Functionally Pooled AutoRegressive model with eXogenous excitation (FP-ARX) [27] and a Vector FP-ARX (VFP-ARX) model [28]. It is noted that various other versions of the FMBM have been presented in the past for damage precise localization [29, 31-36] and precise quantification [31, 37-38] under constant EOCs.

The goal of this study is to investigate, for the first time, the problem of SHM in tendons of a Floating Offshore Wind Turbine (FOWT), taking into account the complete damage diagnosis process (damage detection, damaged tendon identification and damage precise quantification) under varying EOCs. This is achieved through the use of a new version of FMBM [27, 28] that is formulated to operate using just a single response signal received via a single sensor instead of two signals received via two sensors used in [27, 28]. The structure examined in this study is a new concept of a 10 MW multibody FOWT whose tower is supported by an improved and more stable version of the multibody floating platform (TELWIND) [39] consisting of two rigid tanks connected by 12 tendons. The FOWT is subjected to varying EOCs corresponding to seven different WSs, irregular SWHs and current of constant speed and direction, thus reflecting normal and the most severe EOCs of the selected case study site located in the northern coast of Scotland. The FMBM used in this study is based on two types of FMs, a single Functionally Pooled AutoRegressive (FP-AR) model and multiple Vector FP-AR (VFP-AR) models (one per tendon). Due to the dependence of SWH on WS, only the WS is considered as an operating parameter in the FMs. Therefore, the FP-AR model describes the healthy structural dynamics under the effects of varying EOCs of any potential WS and it is used for damage detection. As for the VFP-AR models, each model describes the structural dynamics under the effects of varying EOCs of any potential WS and any damage magnitude on the considered tendon. The VFP-AR models are used for damaged tendon identification and damage precise quantification. It should be noted that the structural complexity of the FMs employed in this study, is significantly reduced, thus offering the advantage for their quick estimation.

In addition, various damage scenarios corresponding to reduced stiffness (%) at a tendon's connection point to the platform's upper tank, are realized. Two of the total 12 tendons are examined in this study, namely, the tendon under the largest tension due to its proximity to the wave direction and an arbitrarily selected tendon being far from the mooring line. It should be noted that the effects of varying EOCs on the healthy FOWT fully "mask" the effects of damages of magnitude less than 20 %. On the other hand, the damages of magnitude [20-80] % have small effects on the structural dynamics due to the high number and robustness of the existing tendons. Additionally, the damages of magnitude [20-80] % on the one tendon under constant EOC, affect the

structural dynamics in a similar manner. The damages of magnitude [10-100] % on different tendons, also have similar effects on the structural dynamics. Thus, these conditions lead to a highly challenging damage diagnosis problem.

Consequently, a numerical model of the coupled FOWT is used for the implementation of damage scenarios and the simulation of healthy and damaged structures under the seven WSs and SWHs. A single underwater accelerometer measures the dominant response, surge (translation movement along axis x) acceleration, within a limited and low frequency bandwidth of [0-5] Hz, corresponding to realistic operating conditions under physical excitation.

The rest of this paper is structured as follows: The FOWT, the varying EOCs, the tendon damages and the simulation details are presented in Section 2. The methodology for damaged tendon diagnosis is presented in Section 3. The damaged tendon diagnosis results are presented in Section 4. The conclusions are presented in Section 5.

2. The FOWT structure, its dynamics, damage scenarios and simulations under varying EOCs

2.1 The 10 MW multibody FOWT structure

The examined structure is a new concept of a 10 MW FOWT, which consists of a tower supported by improved and more stable (with reduced weight) version of the multibody floating platform (TELWIND) developed by Esteyco [40] in the ARCWIND project [39]. The multibody platform consists of a lower tank (LT) and an upper tank (UT) connected by 12 tendons (steel cables) (Figure 1) as opposed to 6 tendons (albeit with changes to tendon properties) on the previous version [39]. Three mooring lines are connected to fairleads attached to the UT's top surface at 14 m below the mean sea level for station-keeping of the platform. Part of the reasons for the increase in tendons is to provide sufficient redundancy of tendons connecting between the upper tank and the lower tank. This further guarantees that the 10 MW FOWT remains safe and stable in the event that a single tendon is broken. With regards to the model properties, the upper tank has a draught of 20.5

m, a mass of $5.31 \cdot 10^6$ kg and a volume of 7399.02 m^3. The draught of the lower tank is 100 m, the mass is $8.72 \cdot 10^6$ kg and the volume equals 7922.92 m^3. The pretension of the 12 tendons is approximately $3 \cdot 10^6$ N.

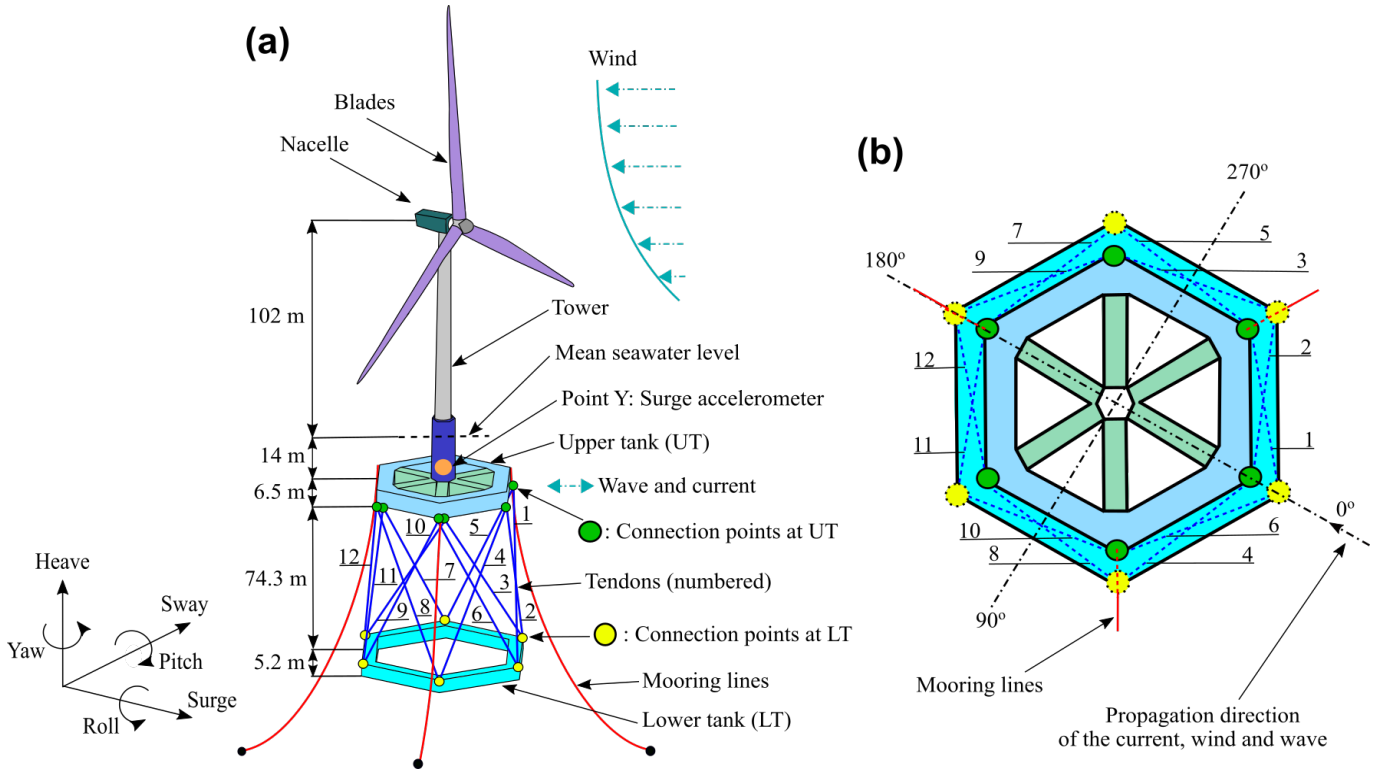

Figure 1. (a) The 10 MW multibody FOWT, the position of the accelerometer (Point Y) and the damage locations which are the connection points at the UT. (b) Bottom view of the platform with the propagation direction of the current, wind and wave.

2.2 The varying EOCs and damage scenarios

In this study, the FOWT is examined under varying EOCs corresponding to seven different WSs 4 m/s, 8 m/s, 11.4 m/s, 14.5 m/s, 18 m/s, 21.5 m/s and 25 m/s with SWHs 1.61 m, 1.67 m, 2.16 m, 2.55 m, 2.95 m, 3.56 m, 4.02 m (Table 1). The FOWT is in a nonoperational state below its cut-in speed of 4 m/s and above a cut-out speed of 25 m/s. The wind is generated via the Kaimal spectrum [41] and a different time series is used as wind excitation to the FOWT for each simulation. Consequently, the same spectral intensity is maintained. The irregular waves are generated via the modified two-parameter Pierson-Moskowitz spectrum [42], [43]. The EOC also includes current of constant speed and direction. Details of the wind, wave and current parameters corresponding to the varying EOCs used in this study, are presented in Table 1 and Figure 1(b). These

parameters represent the characteristics of normal and the most severe EOCs of the selected site located in the northern coast of Scotland.

The healthy scenarios are considered under the seven WSs and SWHs. Each examined damage scenario corresponds to a reduction in the tendon's stiffness (%) at its connection point to the upper tank of the platform under given WS and SWH. The stiffness reduction covers a range of [10-100] % with an increment of 5 %. Tendons 6 and 8 are examined, with tendon 6 suffering the largest tension due to its proximity to the wave direction and tendon 8 randomly selected due to its proximity to a mooring line (Figure 1(b)). WS response for each healthy state is designated as F_w with w being the WS. Equally, each examined damage condition is designated as $F_{w,m}^{q}$ with q = 6, 8 for the examined tendon and m the damage magnitude (% stiffness reduction).

Table 1. Details of the varying EOCs.

Wind speed (WS)	Significant wave height (SWH)	Peak frequency	Propagation direction of sea current, wave, wind	Current speed	Excitation bandwidth
4 m/s	1.61 m	0.285 Hz	0°	0.22 m/s	[0.1-100] Hz
8 m/s	1.67 m	0.199 Hz	0°	0.22 m/s	[0.1-100] Hz
11.4 m/s	2.16 m	0.185 Hz	0°	0.22 m/s	[0.1-100] Hz
14.5 m/s	2.55 m	0.152 Hz	0°	0.22 m/s	[0.1-100] Hz
18 m/s	2.95 m	0.14 Hz	0°	0.22 m/s	[0.1-100] Hz
21.5 m/s	3.56 m	0.121 Hz	0°	0.22 m/s	[0.1-100] Hz
25 m/s	4.02 m	0.112 Hz	0°	0.22 m/s	[0.1-100] Hz

2.3 The simulations

This study uses vibration responses of the 10 MW multibody FOWT under varying EOCs, which correspond to healthy and different damaged states. The responses are obtained from a numerical simulation [44] conducted using F2A, a coupled ANSYS-AQWA and NREL FAST [45]. The platform is modeled as a fully coupled multibody, consisting of two rigid tanks (UT and LT), connected by 12 flexible tendons and kept in station by three mooring lines modelled as nonlinear catenary.

An important consideration in the simulation of the platform is its stability in the event of a tendon failure. The tendons in this concept are designed to have redundancy in the event a tendon or the connection between

159 the upper and the lower tanks fails. The goal is to ensure that the remaining tendons have sufficient reserved
160 capacity to provide stability and support operations. Thus, the FOWT remains safe and stable even if a single
161 tendon is broken. Furthermore, the results of the coupled analysis of a 10 MW multibody FOWT (upper and
162 lower tanks connected by tendons) have shown that this platform remains stable even after the break of a tendon
163 [46]. This is further confirmed by the non-exceedance of the variation range (-15 deg to 15 deg) of the platform's
164 pitch motion response under healthy and damaged states (Figure 2). Further details on the platform's natural
165 frequencies and eigenmodes are available in [8, 46].

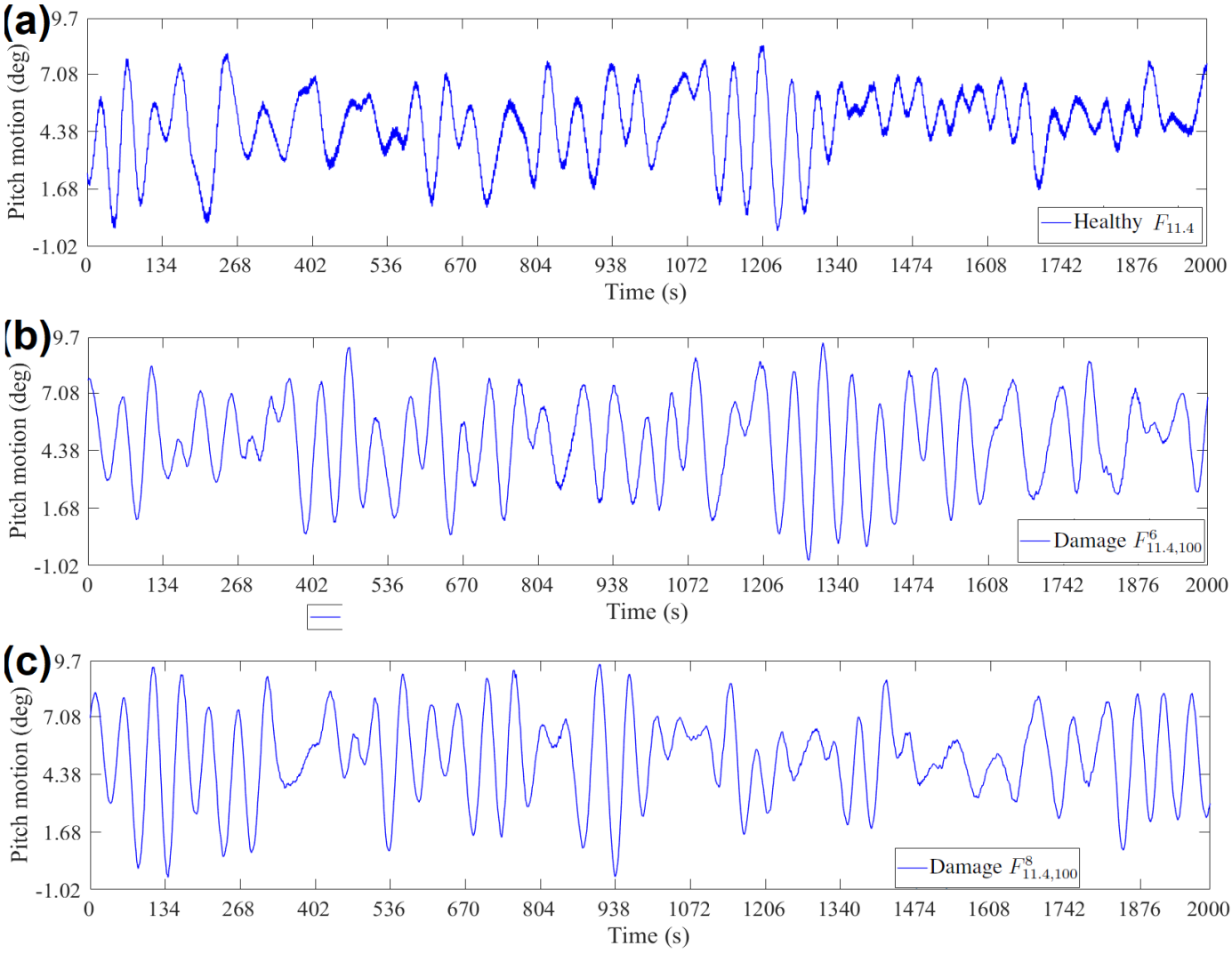

166

167 **Figure 2.** Pitch motion signals from Point Y for the (a) healthy state $F_{11.4}$, (b) the damage state $F^{6}_{11.4,100}$ and (c)
168 the damage state $F^{8}_{11.4,100}$.

169

Although the six degrees of freedom (surge, heave, sway, roll, yaw and pitch) accelerations are measured using a single sensor placed on the UT (Point Y, Figure 1(a)), only the surge acceleration is used in this study. This is because the surge acceleration is determined as the most dominant response. The acceleration signals are sampled at f_s = 10 Hz (acceleration signal bandwidth of [0–5] Hz) with each being N = 20000 samples (2000 s) long.

Similarly, 6 acceleration signals are obtained from each simulation, one for each degree of freedom. A total of 43 simulations are conducted for the healthy structure under the seven WSs (Table 1). A total of 474 simulations are conducted with a single damage for each of the 19 considered magnitudes from each of the two damage locations considered (connection points of tendons 6, 8 at the UT, Figure 1) under each WS. 4 simulations for the healthy structure (one under each of the WSs 4 m/s, 11.4 m/s, 18 m/s, 25 m/s) and 80 simulations for the damaged structure (one per damage magnitude, covering a range of [10-100] % with an increment of 10%, under each of the WSs 4 m/s, 11.4 m/s, 18 m/s, 25 m/s on each of the two tendons) are used in the method's training phase. The remaining 39 simulations of healthy and 394 of damaged structures are solely used in the inspection phase for performance assessments. The 39 simulations correspond to 9 simulations under each of the WSs 4 m/s, 11.4 m/s, 18 m/s, 25 m/s and 1 simulation under each of the WSs 8 m/s, 14.5 m/s, 21.5 m/s. The 394 simulations correspond to i) 2 simulations for each damage magnitude, covering a range of [10-100] % with an increment of 10 %, under each of the WS 4 m/s, 11.4 m/s, 18 m/s, 25 m/s on each of the two tendons, ii) 3 simulations for each damage magnitude, covering a range of [15-95] % with an increment of 5 %, under each of the WS 4 m/s, 11.4 m/s, 18 m/s, 25 m/s on each of the two tendons, iii) 1 simulation for each damage magnitude 10 % and 35 % under WS 8 m/s on each of the two tendons, iv) 1 simulation for each damage magnitude 10 %, 35 %, 55 % and 75 % under WS 14.5 m/s on each of the two tendons, and v) 1 simulation for each damage magnitude 10 %, 35 % and 55 % under WS 21.5 m/s on each of the two tendons. Each signal is sample mean corrected and scaled by its sample standard deviation. Details of the simulations and measured signals, are presented in Table 2.

2.4 Effects of damage and varying EOCs on the FOWT dynamics

The dynamics of the FOWT under the healthy state, vary due to the variability of the WS. This is confirmed through discrepancies between the PSDs estimated via the Welch estimator [47] (Welch estimation details:

Table 2. Details of the performed simulations and vibration signals.

Structural state	Description	No. of damaged tendons	No. of damage magnitudes	No of WSs	No. of simulations – Baseline phase	No. of simulations – Inspection phase
Healthy	-		-	7	4 (one under each WS [4, 11.4, 18, 25] m/s)	36 (9 under each WS [4, 11.4, 18, 25] m/s) 3 (1 under each WS [8, 14.5, 21.5] m/s)
Damaged	Reducing the stiffness of a single tendon (%) (increment of 5%)	2 (Tendons 6, 8)	19	7	80 (one per damage magnitude [10, 20, 30, 40, …., 100] % under each WS [4, 11.4, 18, 25] m/s on each tendon)	394 (2 per damage magnitude [10, 20, 30, …., 100] % under each WS [4, 11.4, 18, 25] m/s on each tendon) (3 per damage magnitude [15, 25, 35, …., 95] % under each WS [4, 11.4, 18, 25] m/s on each tendon) (1 per damage magnitude [10, 35] % under WS [8] m/s on each tendon) (1 per damage magnitude [10, 35, 55, 75] % under WS [14.5] m/s on each tendon) (1 per damage magnitude [10, 35, 55] % under WS [21.5] m/s on each tendon)
Sampling frequency: f_s = 10 Hz, acceleration signal bandwidth: [0-5] Hz Signal length: N = 20000 samples (2000 s)						

Matlab function *pwelch.m*; signal length 20000 samples, window length 868 samples, 95% overlap, Hamming window, frequency resolution of 0.011 Hz) and corresponding to the healthy state under the four WSs 4 m/s, 11.4 m/s, 18 m/s, 25 m/s, in Figure 3. The discrepancies are evident in the bandwidths of [0.04-0.3] Hz and [1.05-1.2] Hz. Moreover, in Figure 4, the effects of selected damage cases on the structural dynamics, are shown via Welch-based (Welch estimation details: Matlab function *pwelch.m*; signal length 20000 samples, window

868 samples, 95% overlap, Hamming window, frequency resolution of 0.011 Hz) PSD estimates corresponding to the healthy structure and the structure under 3 damage magnitudes 10 %, 20 %, 80% on tendon 6 and under the four WSs. In Figure 4(a), the PSDs of the healthy and damaged structure under damage of magnitude 10 %, overlap throughout the frequency bandwidth. In Figures 4(b)-(c), the PSDs of the healthy and damaged structure under damage of magnitudes 20 %, 80 %, overlap extensively for most of the frequency bandwidth. Deviations between the healthy and damaged structural dynamics are noticed in bandwidth of [0.85-1.2] Hz for magnitude 20 % (Figure 4(b)) and in bandwidths of [0.5-0.6] Hz and [0.85-1.2] Hz for magnitude 80 % (Figure 4(c)). It is noted that similar changes on the dynamics are observed for damages on tendon 8. Based on these results, it is evident that the effects of varying WS on the healthy FOWT dynamics, fully 'mask' the effects of damages of magnitude less than 20 %. Furthermore, small deviations (less than 0.1 Hz) between the healthy and damaged structural dynamics exist for magnitude [20-80] % due to the robustness and high number of the existing tendons. Hence, it is confirmed by the deviations corresponding to damage magnitude [10-80] % that these damages have small effects on the structural dynamics and that damage detection is quite challenging.

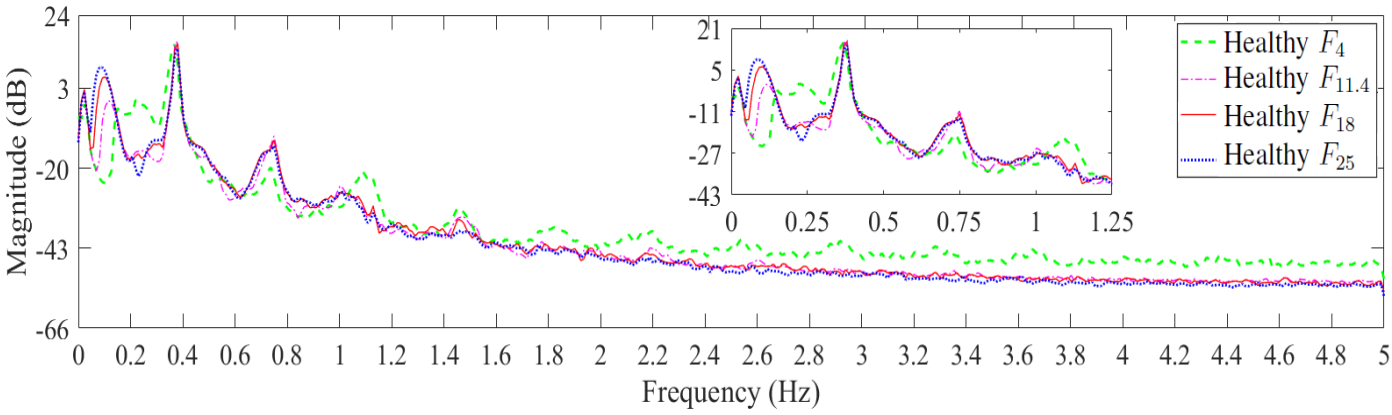

Figure 3. Welch-based PSD estimates using surge acceleration signals from Point Y for the healthy FOWT under the four considered WSs 4 m/s, 11.4 m/s, 18 m/s, 25 m/s.

In Figure 5, a comparison of Welch-based (Welch estimation details: Matlab function *pwelch.m*; signal length 20000 samples, window 868 samples, 95% overlap, Hamming window, frequency resolution of 0.011 Hz) PSD estimates corresponding to damage of magnitudes 20 %, 40 %, 60 %, 80 % on tendons 6 for WSs 11.4 m/s, 25 m/s and on tendon 8 for WSs 4 m/s, 18 m/s, is presented. The effects of these damages differ in

bandwidths of [0.27-.34] Hz, [0.5-0.6] Hz and [0.85-1.1] Hz for WS 4 m/s (Figure 5(a)) and in bandwidths of [0.23-0.34] Hz, [0.5-0.6] Hz, [0.64-0.78] Hz, [0.85-1.07] Hz for WSs 11.4 m/s (Figure 5(b)), 18 m/s (Figure 5(c)) and 25 m/s (Figures 5(d)). It is obvious that the differences between these damages under constant WS, are less than 0.23 Hz which is quite small. These small differences mean that damages of magnitude [20-80] % under constant WS, similarly affect the structural dynamics due to the robustness and number of the existing tendons. Also, similar effects indicate that damaged tendon identification and damage precise quantification are highly challenging.

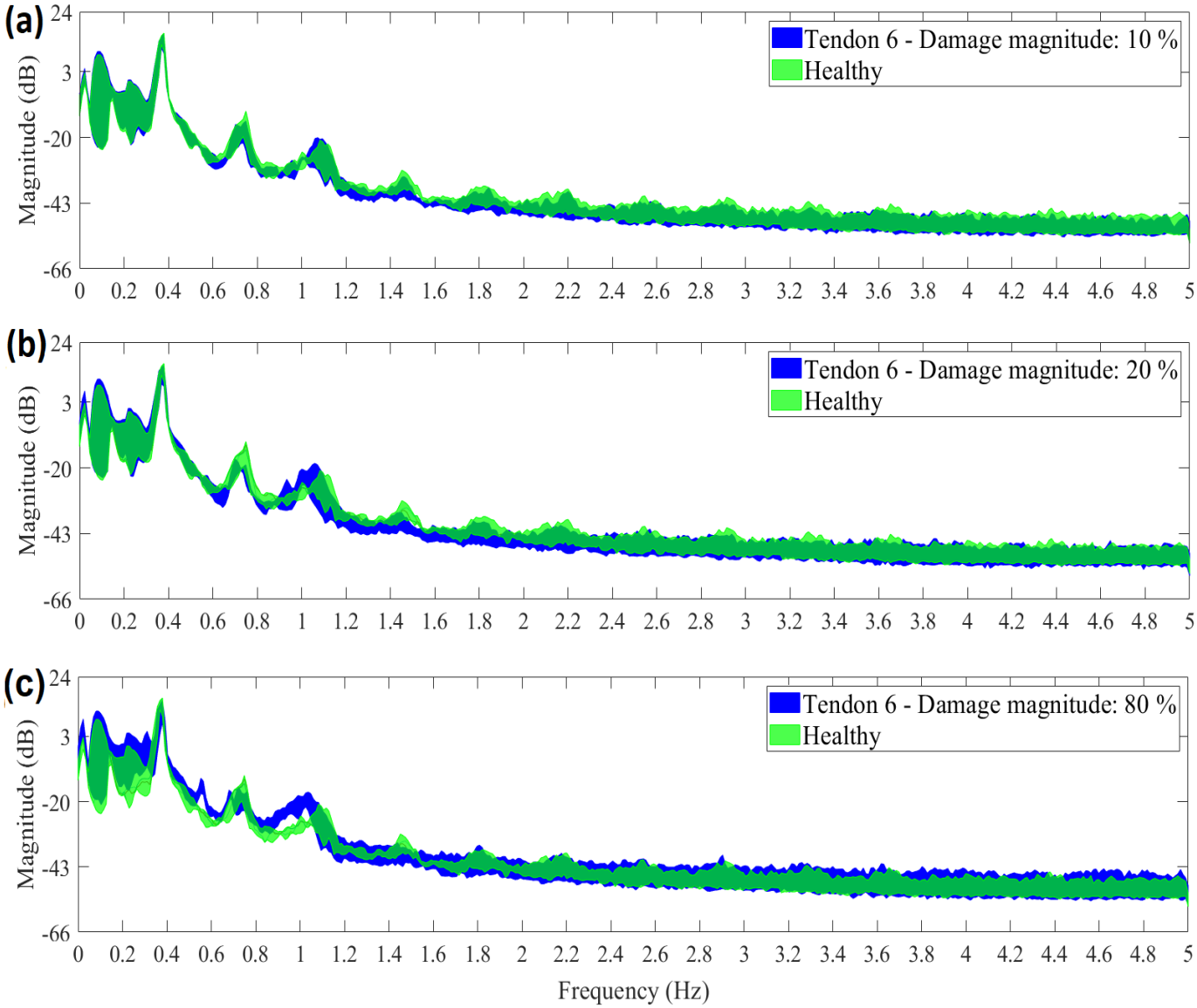

Figure 4. Welch-based PSD estimates using surge acceleration signals from Point Y for the healthy and the damaged FOWT for the four WSs 4 m/s, 11.4 m/s, 18 m/s, 25 m/s, with damages on tendon 6 and of magnitudes (a) 10 %, (b) 20 % and (c) 80 %.

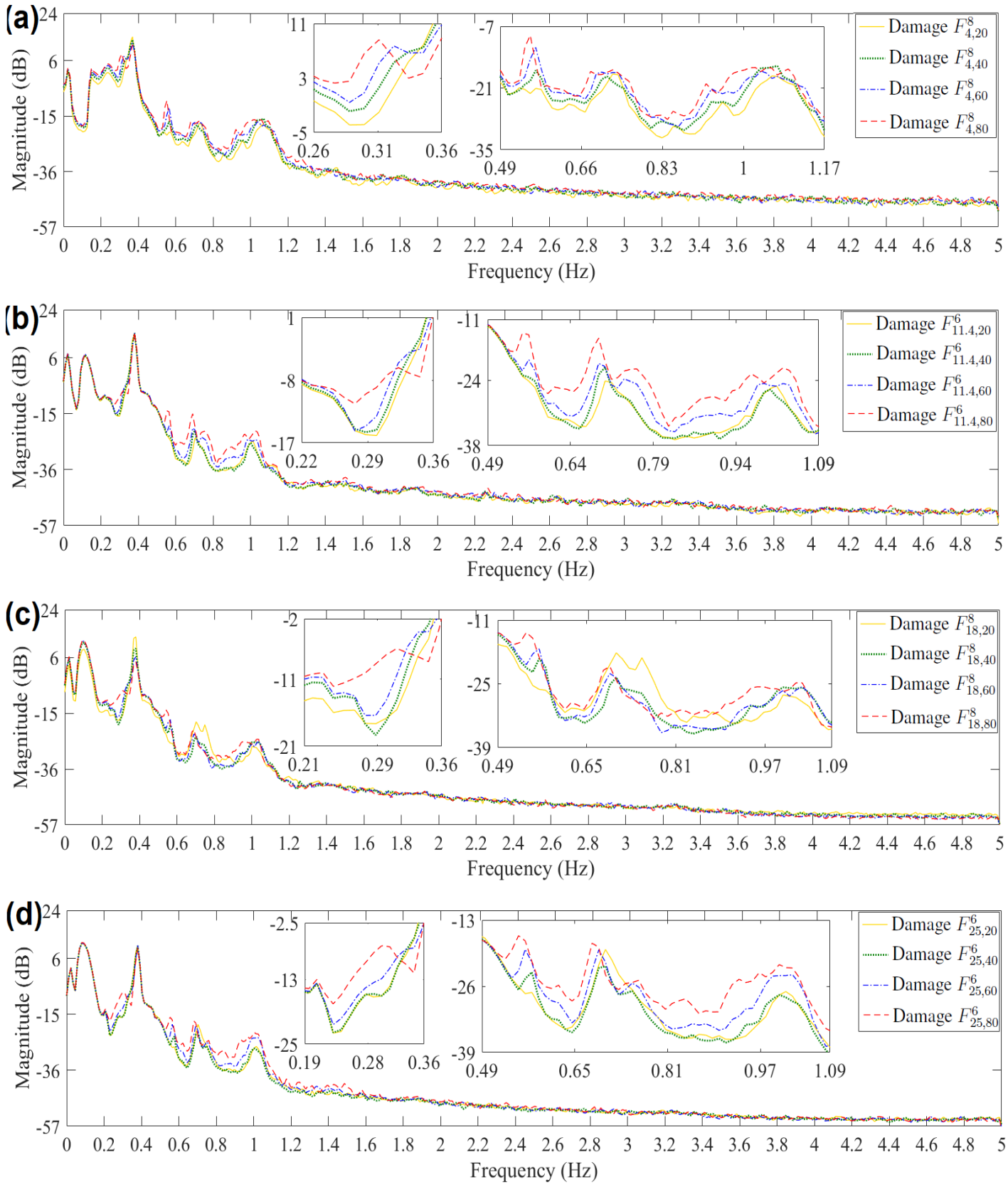

Figure 5. Welch-based PSD estimates using surge acceleration signals from Point Y for the FOWT with damage of magnitudes 20 %, 40 %, 60 %, 80% on (b),(c) tendon 6 for WS 11.4 m/s, 25 m/s and (a),(c) tendon 8 under WS 4 m/s, 18 m/s.

The difficulty of damaged tendon identification and damage precise quantification is also revealed by the similarity in the effects of damages on different tendons. This similarity is confirmed through additional comparisons between the Welch-based (Welch estimation details: Matlab function *pwelch.m*; signal length 20000 samples, window 868 samples, 95% overlap, Hamming window, frequency resolution of 0.011 Hz) PSD estimates for some of the considered damage cases under the four WSs 4 m/s, 11.4 m/s, 18 m/s and 25 m/s, presented in Figure 6. For each pair of the compared damage cases (damages of magnitude 10 % on tendons 6, 8 and damages of magnitude 40 % on tendons 6, 8), the corresponding PSDs almost coincide with each other.

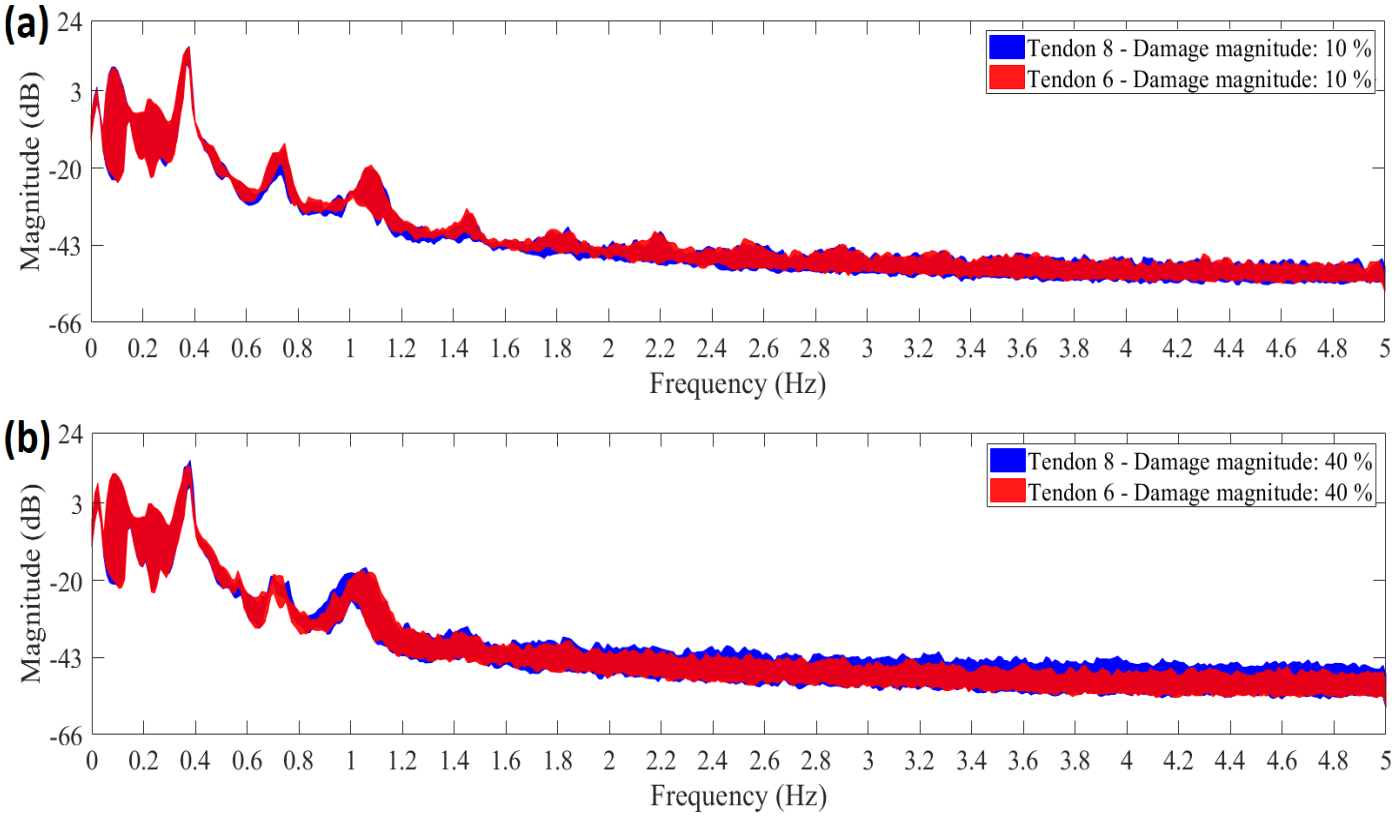

Figure 6. Comparison between Welch-based PSD estimates using surge acceleration signals from Point Y for damages on tendons 6, 8 and of the same magnitude for the four considered WSs 4 m/s, 11.4 m/s, 18 m/s, 25 m/s: (a) Magnitude 10 % and (b) magnitude 40 %.

3. Damaged tendon diagnosis method

In this study, the formulation of the new version of the FMBM [27, 28] based on a single response signal received from a single sensor instead of two signals received via two sensors as in [27, 28], is presented for

damage diagnosis of tendons of a FOWT under varying EOCs. Due to the dependence of SWH on WS, only the WS is considered as an operating parameter in the FMs. In step 1 of the method, damage detection is achieved based on a single FP-AR model and damaged tendon identification and damage precise quantification (steps 2 and 3) are achieved based on multiple VFP-AR models (one per tendon). The method consists of two phases, the baseline phase and the inspection phase. The baseline (training) phase is performed based on data from known structural states and when the structure is not operational (shutdown condition). The inspection phase runs periodically or continuously during the structure's normal operation (on-line) based on current vibration data, while the structure is under unknown health state.

3.1 Baseline phase

Initially, a FP-AR model [8] having the ability to represent the (partial) dynamics of the healthy FOWT under varying EOCs of any potential WS, is identified. For identifying the FP-AR model, M_1 response signals corresponding to a sample of the considered WSs, are acquired. These sampled WSs cover the range $[w_{min}, w_{max}]$ via the discretization $w_v \in w_1, w_2, \dots, w_{M_1}$ and each response signal is characterized by a specific WS w_v. Thus, for each WS, the following operating parameter k is defined as $k = w_v \Leftrightarrow k_v$ with $v = 1, \dots, M_1$ and a pool of M_1 response signals $y_k[t]$, each of length N, is obtained with $t = 1, \dots, N$.

Based on the pool of the acquired response signals, a mathematical description of the healthy structural (partial) dynamics under varying EOCs of any potential WS, is obtained through a FP-AR$(na)_p$ model of the following form [8]:

$$y_k[t] + \sum_{i=1}^{na} \alpha_i(k) \cdot y_k[t-i] = e_k[t] \quad \text{with} \quad e_k[t] \sim \text{iid}\, \mathcal{N}\left(0, \sigma_e^2(k)\right) \quad \text{and} \quad k \in R \tag{1}$$

$$a_i(k) = \sum_{j=1}^{p} a_{i,j} \cdot G_j(k) \tag{2}$$

with na designating the AutoRegressive (AR) order, $y_k[t]$ the response signal and $e_k[t]$ the disturbance (residual) signal that is white (serially uncorrelated) zero-mean with variance $\sigma_e^2(k)$. iid stands for identically

independently distributed and $\mathcal{N}(\cdot,\cdot)$ designates normal distribution with the indicated mean and variance. Based on Equation (2), the AR parameters $a_i(k)$ are functions of k belonging to a p-dimensional functional subspace spanned by the (mutually independent) functions $G_1(k), G_2(k), \dots, G_p(k)$ (functional basis). The latter are univariate (one variable) orthogonal polynomials (Chebyshev, Legendre and other families) forming a functional basis $\mathcal{G}$ [8, 37]. The constants $a_{i,j}$ designate the AR projection coefficients which can be formed in the vector $\boldsymbol{\theta} = \left[a_{1,1} \dots a_{na,p}\right]^T_{[na\cdot p\times 1]}$ (bold-face upper/lower case symbols designate matrix/column-vector quantities, respectively; ^{T} designates transposition).

The FP-AR$(na)_p$ model (Equations (1), (2)) is re-written in a linear regression form (see details in [33, 36, pp. 28-31, 37]):

$$y_k[t] = [\boldsymbol{\varphi}_k^T[t] \otimes \boldsymbol{g}^T(k)] \cdot \boldsymbol{\theta} + e_k[t] = \boldsymbol{\phi}_k^T[t] \cdot \boldsymbol{\theta} + e_k[t] \tag{3}$$

with $\boldsymbol{\varphi}_k[t] = \left[-y_k[t-1] \dots -y_k[t-na]\right]^T_{[na\times 1]}$ designating the regression vector, $\boldsymbol{g}(k) = \left[G_1(k) \dots G_p(k)\right]^T_{[p\times 1]}$ the functional basis vector and $\otimes$ the Kronecker product.

Pooling together Equation (3) of the FP-AR model corresponding to the various operating parameters $k\left(k_1, k_2, \dots, k_{M_1}\right)$ of the obtained M_1 response signals for a single value of t, leads to:

$$\begin{bmatrix} y_{k_1}[t] \\ \vdots \\ y_{k_{M_1}}[t] \end{bmatrix}_{[M_1\times 1]} = \begin{bmatrix} \boldsymbol{\phi}_{k_1}^T[t] \\ \vdots \\ \boldsymbol{\phi}_{k_{M_1}}^T[t] \end{bmatrix}_{[M_1\times p\cdot na]} \cdot \boldsymbol{\theta} + \begin{bmatrix} e_{k_1}[t] \\ \vdots \\ e_{k_{M_1}}[t] \end{bmatrix}_{[M_1\times 1]} \Longrightarrow \boldsymbol{y}[t] = \boldsymbol{\Phi}[t] \cdot \boldsymbol{\theta} + \boldsymbol{e}[t] \tag{4}$$

Then, the data for $t = 1, \dots, N$ are substituted in Equation (4) for the estimation of the parameter vector $\boldsymbol{\theta}$ through the Ordinary Least Squares (OLS) estimator [33, 36, p. 15] (a hat ˆ above a quantity designates its estimate):

$$\widehat{\boldsymbol{\theta}} = [\textstyle\sum_{t=1}^{N} \boldsymbol{\Phi}^T[t]\, \boldsymbol{\Phi}[t]]^{-1} \cdot [\sum_{t=1}^{N} \boldsymbol{\Phi}^T[t]\, \boldsymbol{y}[t]] \tag{5}$$

The order of the FP-AR model is determined through a conventional AR(*na*) model [48, pp. 81-83] based on a single response signal from the healthy structure under one of the considered WS values. The minimization of the Bayesian Information Criterion (BIC) [48, pp. 505-507] leads to the selection of the order

of the AR model. The determination of the FP-AR model's functional subspace p, given a selected orthogonal polynomial family, is achieved via a Genetic Algorithm (GA) procedure [33, 36, p. 16, 49] based on the minimization of an extended version of the BIC [36, pp. 33-35, 50].

FP-AR model's validation is achieved through the verification of the uncorrelatedness (whiteness) of the model's residual signals. The whiteness check is conducted based on the Pena-Rodriguez test [36, p. 19, 51] which detects changes in the partial autocorrelation function $\pi_e[\tau]$ ($\tau = 1, \dots, h$ is the lag) [52, pp. 64-68] of the residual signals. The Pena-Rodriguez test is based on a D statistic which is a function of $\pi_e[\tau]$ and it follows a standard normal distribution $\mathrm{D} \sim \mathcal{N}(0,1)$. A signal's whiteness is confirmed only if D does not exceed the critical limits of the distribution, $-Z_{1-\alpha} \leq \mathrm{D} \leq Z_{1-\alpha}$ ($-Z_{1-\alpha}$, $Z_{1-\alpha}$ the critical limits, α the risk level).

A VFP-AR [28, 31, 33, 36, pp. 13-16, 53] model having the ability to represent the FOWT (partial) dynamics under varying EOCs of any potential WS and damage of any magnitude at the location of interest on a single tendon, is identified for each examined tendon. For identifying the VFP-AR model, M_3 response signals are obtained for a sample of the considered WSs (the same WSs with those considered in the FP-AR model) and a sample of different damage magnitudes on the examined tendon. These sampled WSs and damage magnitudes cover the range $[w_{min}, w_{max}] \times [m_{min}, m_{max}]$ via the discretizations $w_v \in w_1, w_2, \dots, w_{M_1}$ and $m_l \in m_1, m_2, \dots, m_{M_2}$ with $M_3 = M_1 \times M_2$. Each signal is characterized by a specific pair of WS w_v and magnitude m_l. Thus, for a pair of WS and damage magnitude, the following operating parameter vector $\boldsymbol{k}$ is defined as $\boldsymbol{k} = [w_v \ m_l]^T \Leftrightarrow \boldsymbol{k}_{v,l}$ with $v = 1, \dots, M_1$ and $l = 1, \dots, M_2$ and a pool of M_3 response signals $y_{\boldsymbol{k}}[t]$, each of length N, is obtained with $t = 1, \dots, N$.

Based on this pool of data, a mathematical description of the structural (partial) dynamics under varying EOCs of any potential WS and damage of any potential magnitude on the examined tendon, is obtained through a VFP-AR$(na)_p$ model of the following form [28, 31, 33, 36, pp. 13-16, 53]:

$$y_{\boldsymbol{k}}[t] + \sum_{i=1}^{na} \alpha_i(\boldsymbol{k}) \cdot y_{\boldsymbol{k}}[t-i] = e_{\boldsymbol{k}}[t] \quad \text{with} \quad e_{\boldsymbol{k}}[t] \sim \text{iid}\, \mathcal{N}\left(0, \sigma_e^2(\boldsymbol{k})\right) \quad \text{and} \quad \boldsymbol{k} \in R^2 \tag{6}$$

$$a_i(\boldsymbol{k}) = \sum_{j=1}^{p} a_{i,j} \cdot G_j(\boldsymbol{k}) \tag{7}$$

with $y_{\boldsymbol{k}}[t]$ being the response signal and $e_{\boldsymbol{k}}[t]$ being the disturbance (residual) signal that is essentially a white (serially uncorrelated) zero-mean with variance $\sigma_e^2(\boldsymbol{k})$. Based on Equation (7), the AR parameters $a_i(\boldsymbol{k})$ are functions of $\boldsymbol{k}$ belonging to a p-dimensional functional subspace spanned by the (mutually independent) functions $G_1(\boldsymbol{k}), G_2(\boldsymbol{k}), \dots, G_p(\boldsymbol{k})$ (functional basis). The latter are bivariate (two variables) orthogonal polynomials forming a functional basis $\mathcal{G}$ [31, 33, 34, 36, p. 28]. Based on the M_3 response signals corresponding to the various operating parameter vectors $\boldsymbol{k}\left(\boldsymbol{k}_{1,1}, \boldsymbol{k}_{2,1}, \dots, \boldsymbol{k}_{M_1,M_2}\right)$, the vector of projection coefficients $\boldsymbol{\theta}$ (Equation (6)) is estimated based on the OLS estimator (Equation (5)) (for more details see [33, 36, p. 15]).

For the selection of the VFP-AR model orders, the determination of the model's functional subspace dimensionality p and the model validation, the same procedures are followed as in the FP-AR model identification (see also in [33, 36, p. 16]).

Remark: For simplicity of notation, the same symbols na, p, $\boldsymbol{\theta}$ are commonly used in the FP-AR and VFP-AR models without necessarily being equal. They are separately obtained as described in the above identification procedures.

3.2 Inspection phase

Step 1: Damage detection. A response $y_u[t]$ signal is obtained under the current (unknown) structural state. Then the signal is driven through the FP-AR$(na)_p$ model (Equation (1)) which is re-parametrized in terms of the currently unknown state, $k = w$:

$$y_u[t] + \sum_{i=1}^{na} a_i(k) \cdot y_u[t-i] = e_u[t,k] \tag{8}$$

The estimation of k is achieved based on the following Nonlinear Least Squares (NLS) estimator [28, 33, 36, pp. 16-17, 37, 38] (realized via golden search and parabolic interpolation [54]):

$$\hat{k} = \arg\min_{k \in K} \sum_{t=1}^{N} e_u^2[t,k], \qquad \hat{\sigma}_{e_u}^2 = \frac{1}{N}\sum_{t=1}^{N} e_u^2\left[t,\hat{k}\right] \tag{9}$$

with $e_u[t,k]$ provided by Equation (8) and $K=[w_{min},w_{max}]$ the boundaries of the examined WS range. The estimate $\hat{k}$ is asymptotically ($N\to\infty$) normally distributed with mean μ_k and variance σ_k^2, that is $\hat{k}\sim\mathcal{N}(\mu_k,\sigma_k^2)$.

Then damage detection is accomplished by checking the validity of estimate $\hat{k}$. The latter is accepted as valid only when the residual signal $e_u[t,\hat{k}]$ uncorrelatedness (whiteness) is confirmed via the Portmanteau Test [28, 37, 38] which detects changes in the normalized autocorrelation function $\rho[\tau]$ ($\tau=1,\dots,h$ is the lag) [51, pp. 21-26] of $e_u[t,\hat{k}]$. The Portmanteau Test is based on a Q statistic which is a function of $\rho[\tau]$ and it follows a chi-square distribution $\mathrm{Q}\sim\chi_h^2$. A signal's whiteness is confirmed only if Q does not exceed the critical limit of the distribution, $\mathrm{Q}\le\chi_{1-\alpha,h}^2$ ($\chi_{1-\alpha,h}^2$ the critical limit, α the risk level). The non-acceptance of the $\hat{k}$ validity means that a damage is detected, otherwise the examined structural state is healthy.

Step 2: Damaged tendon identification. After the detection of a damage, the signal $y_u[t]$ is driven through each (baseline phase) VFP-AR model (one model per examined tendon; Equation (6)) which is now re-parametrized in terms of the currently unknown state, $\boldsymbol{k}=[w\ m]^T$:

$$y_u[t]+\sum_{i=1}^{na}a_i(\boldsymbol{k})\cdot y_u[t-i]=e_u[t,\boldsymbol{k}] \tag{10}$$

The estimation of $\boldsymbol{k}$ is achieved based on the following Nonlinear Least Squares (NLS) estimator [28, 31, 33, 36, p. 18]:

$$\widehat{\boldsymbol{k}}=\arg\min_{\boldsymbol{k}\in K}\sum_{t=1}^{N}e_u^2[t,\boldsymbol{k}]\,,\qquad \hat{\sigma}_{e_u}^2=\frac{1}{N}\sum_{t=1}^{N}e_u^2[t,\widehat{\boldsymbol{k}}] \tag{11}$$

with $e_u[t,\boldsymbol{k}]$ provided by Equation (10) and $K=[w_{min},w_{max}]\times[m_{min},m_{max}]$ including the boundaries of the examined WS and magnitude ranges. The minimization in Equation (11) is achieved via a GA, followed by a refinement via Sequential Quadratic Programming (SQP) techniques [55]. The estimate $\widehat{\boldsymbol{k}}$ is asymptotically ($N\to\infty$) normally distributed with mean $\boldsymbol{\mu_k}$ and covariance matrix $\boldsymbol{\Sigma_k}$, that is $\widehat{\boldsymbol{k}}\sim\mathcal{N}(\boldsymbol{\mu_k},\boldsymbol{\Sigma_k})$.

The validity of the estimate $\widehat{\boldsymbol{k}} = [\widehat{w}\ \ \widehat{m}]^T$ based on the VFP-AR model for the examined tendon, is accepted only when the uncorrelatedness (whiteness) of the residual signal $e_u[t, \widehat{\boldsymbol{k}}]$ is confirmed via the Pena-Rodriguez test. The whiteness of the residual signal is confirmed only if the D statistic does not exceed the critical limits of the normal distribution (see subsection 3.1). The acceptance of the validity means that the VFP-AR model is able to represent the structural dynamics under the current damage and that the examined tendon is identified as the damaged tendon. It should be noted that if the above procedure underlines that the estimate $\widehat{\boldsymbol{k}}$ belongs to two or more tendons, the one with the lowest D statistic is selected as the actual damaged tendon. If $e_u[t, \widehat{\boldsymbol{k}}]$ is not white then an alternative VFP-AR model (representing a different tendon) shall be checked.

Step 3. Damage precise quantification. If the examined tendon has been successfully identified as the damaged tendon, then the estimate $\widehat{\boldsymbol{k}} = [\widehat{w}\ \ \widehat{m}]^T$ is accepted. The estimated magnitude of the examined damage on the identified damaged tendon is $\widehat{m}$ under an estimated WS $\widehat{w}$. Therefore, confidence intervals for $\widehat{w}$, $\widehat{m}$ are constructed [31, 35, 36, p. 18, 37, 38] as:

$$\left[\widehat{w} - t_{1-\frac{\alpha}{2},N-1} \cdot \hat{\sigma}_w,\ \widehat{w} + t_{1-\frac{\alpha}{2},N-1} \cdot \hat{\sigma}_w\right],\ \ \left[\widehat{m} - t_{1-\frac{\alpha}{2},N-1} \cdot \hat{\sigma}_m,\ \widehat{m} + t_{1-\frac{\alpha}{2},N-1} \cdot \hat{\sigma}_m\right] \tag{12}$$

with $-t_{1-\frac{\alpha}{2},N-1}$ and $t_{1-\frac{\alpha}{2},N-1}$ designating the t distribution's (with $N-1$ degrees of freedom) critical limits, α the risk level and $\hat{\sigma}_w, \hat{\sigma}_m$ the square roots of the first and second diagonal components of the estimated covariance matrix $\widehat{\boldsymbol{\Sigma}}_{\boldsymbol{k}}$ provided by the Cramer-Rao lower bound [31, 33, 36, p. 18].

4. Damaged tendon diagnosis method

4.1 Baseline phase

An AR(171) model is identified based on a response signal from the healthy structure under WS 11.4 m/s (see details in Table 3). The order of the conventional AR model is adopted as the order of a FP-AR model representing the healthy structural dynamics under varying EOCs of any potential WS. $M_1 = 4$ response signals

402 **Table 3**. Details of the FMBM.

Baseline phase

State	Tendon	Signal length	Estimated model	No. of signals	No. of projection coefficients	Sample per Parameter	Condition number[a]	BIC
Healthy	-	N =20000 samples	AR(171)	$M = 1$	-	116.59	$5.88 \cdot 10^6$	-8.18
Healthy	-	N =20000 samples	FP-AR$(171)_4$	$M_1 = 4$	513	155.94	$2.16 \cdot 10^7$	-32.02
Damaged	6	N =20000 samples	VFP-AR$(171)_9$	$M_3 = 40$	1539	519.81	$5.59 \cdot 10^7$	-317.24
Damaged	8	N =20000 samples	VFP-AR$(171)_9$	$M_3 = 40$	1539	519.81	$1.81 \cdot 10^8$	-321.48

Order selection based on an AR model: Estimation method*:* OLS, Matlab function: *arx.m*

Functional subspace dimensionality determination based on Genetic Algorithm: population=100, elite count 20, crossover fraction=0.7, maximum number of generations=100, Tolerance of the objective function $= 10^{-4}$; Matlab function: *ga.m*

FP-AR(171)$_4$ model's functional basis: p_1=4 univariate Shifted Legendre polynomials: $\mathcal{G}_1 = [G_0(k)\ \ G_1(k)\ \ G_2(k)\ \ G_3(k)\ ]^b$

VFP-AR(171)$_9$ model's functional basis (tendon 6): p_2=9 bivariate Shifted Legendre polynomials:

$$\mathcal{G}_2 = \left[G_{0,0}(\boldsymbol{k})\ \ G_{0,1}(\boldsymbol{k})\ \ G_{0,2}(\boldsymbol{k})\ \ G_{1,0}(\boldsymbol{k})\ \ G_{1,1}(\boldsymbol{k})\ \ G_{1,2}(\boldsymbol{k})\ \ G_{2,0}(\boldsymbol{k})\ \ G_{2,1}(\boldsymbol{k})\ \ G_{3,0}(\boldsymbol{k})\right]^c$$

VFP-AR(171)$_9$ model's functional basis (tendon 8): p_2=9 bivariate Shifted Legendre polynomials:

$$\mathcal{G}_2 = \left[G_{0,0}(\boldsymbol{k})\ \ G_{0,1}(\boldsymbol{k})\ \ G_{0,2}(\boldsymbol{k})\ \ G_{1,0}(\boldsymbol{k})\ \ G_{1,1}(\boldsymbol{k})\ \ G_{2,0}(\boldsymbol{k})\ \ G_{2,1}(\boldsymbol{k})\ \ G_{3,0}(\boldsymbol{k})\ \ G_{3,9}(\boldsymbol{k})\right]^c$$

Validation method: Pena-Rodriguez test with risk levels $\alpha = 4 \times 10^{-1}$ (FP-AR$(171)_4$ model), $\alpha = 4.4 \times 10^{-1}$ (VFP-AR$(171)_9$ model – tendon 6),), $\alpha = 4.4 \times 10^{-1}$ (VFP-AR$(171)_9$ model – tendon 8) & no. of lags = 2100

Inspection phase – Step 1: Damage detection

FP-AR model based estimation of k : NLS estimator based on golden search & parabolic interpolation (Tolerance of the objective function $= 10^{-10}$; Tolerance of the estimated value $= 10^{-10}$; Matlab function: *fminbnd.m*)

Validation method: Portmanteau test with no. of lags = 950

Inspection phase – Step 2: Damaged tendon identification & Step 3: Damage precise quantification

VFP-AR models based estimation of $\boldsymbol{k}$: NLS estimator based on Genetic Algorithm (tolerance of the objective function = 10−10; Matlab function: ga.m) and Sequential Quadratic Programming (tolerance of the objective function $= 10^{-10}$; tolerance of the estimated value $= 10^{-10}$; Matlab function: *fmincon.m*).

Validation method: Pena-Rodriguez test with no. of lags = 2100

[a] Condition number of $\sum_{t=1}^{N} \boldsymbol{\Phi}^T[t]\,\boldsymbol{\Phi}[t]$ in Equation (5).

[b] $G_i(k)$: univariate orthogonal polynomial of degree i .

[c] $G_{i,j}(\boldsymbol{k})$: bivariate orthogonal polynomial of total degree $i + j$, obtained as tensor product from two univariate polynomials $G_i(w)$, $G_j(m)$ of degrees i, j, respectively.

403

404 are used for identifying a FP–AR model with WS considered in the WS range $w_v \in [4, 25]$ m/s and the range
405 covered via the discretization $w_v \in [4, 11.4, 18, 25]$ m/s (see subsection 3.1). The FP–AR model's functional
406 subspace dimensionality p_1 is determined via a GA-based procedure based on the minimization of BIC. The
407 initial functional subspace is selected to be spanned by 4 univariate Shifted Legendre polynomials which are
408 functions of the WS w_v normalized with respect to the maximum value that is $w_v = w_v/25 \quad [0, 1]$.

409 The identification procedure leads to a FP-AR model. A comparison between the Welch-based (Welch
410 estimation details: Matlab function *pwelch.m*; signal length 20000 samples, window 868 samples, 95% overlap,
411 Hamming window, frequency resolution of 0.011 Hz) and the FP-AR model's PSD estimates, is presented in
412 Figure 7. The agreement between the PSDs shows the high accuracy in modelling the healthy structural
413 dynamics under varying EOCs. The dependence of an indicative FP-AR model parameter as a function
414 of WS, is depicted in Figure 8(a). The FP-AR model based PSD magnitude as a function of frequency
415 and WS, is depicted in Figure 8(b). Full details on the FP-AR model identification are presented in Table 3.

416 Subsequently, for each examined tendon, $M_3 = 40$ response signals are used for identifying a VFP–AR
417 model. This model represents the structural dynamics under varying EOCs of any potential WS in the WS range
418 $w_v \in [4, 25]$ m/s and under any damage magnitude on the tendon in the damage magnitude range $m_l \in [10,$
419 100] % (see subsection 3.1). The WS range is covered via the discretization $w_v \in [4, 11.4, 18, 25]$ m/s and the
420 magnitude range is covered via the discretization $m_l \in [10, 20, 30, \ldots., 80, 90, 100]$ %. The AR model order is
421 selected based on the AR(171) model. Then the dimensionality of the functional subspace p_2 of the VFP–AR
422 model, is determined via a GA-based procedure based on the minimization of BIC. The initial functional
423 subspace is spanned by 40 bivariate Shifted Legendre polynomials which are functions of the WS w_v and the
424 magnitude m_l normalized with respect to the corresponding maximum values that are $w_v = w_v/25 \quad [0, 1]$ and
425 $m_l = m_l/100 \quad [0, 1]$.

426 Two VFP-AR models are identified for tendons 6 and 8. The dependence of indicative VFP-AR
427 models parameters as a function of WS and damage magnitude, is depicted in Figure 9. PSD magnitudes of the

two VFP-AR models as a function of frequency and WS, are depicted in Figures 10(a),(b) and of frequency and damage magnitude in Figure 10(c),(d). Full details on the VFP-AR models identification are presented in Table 3.

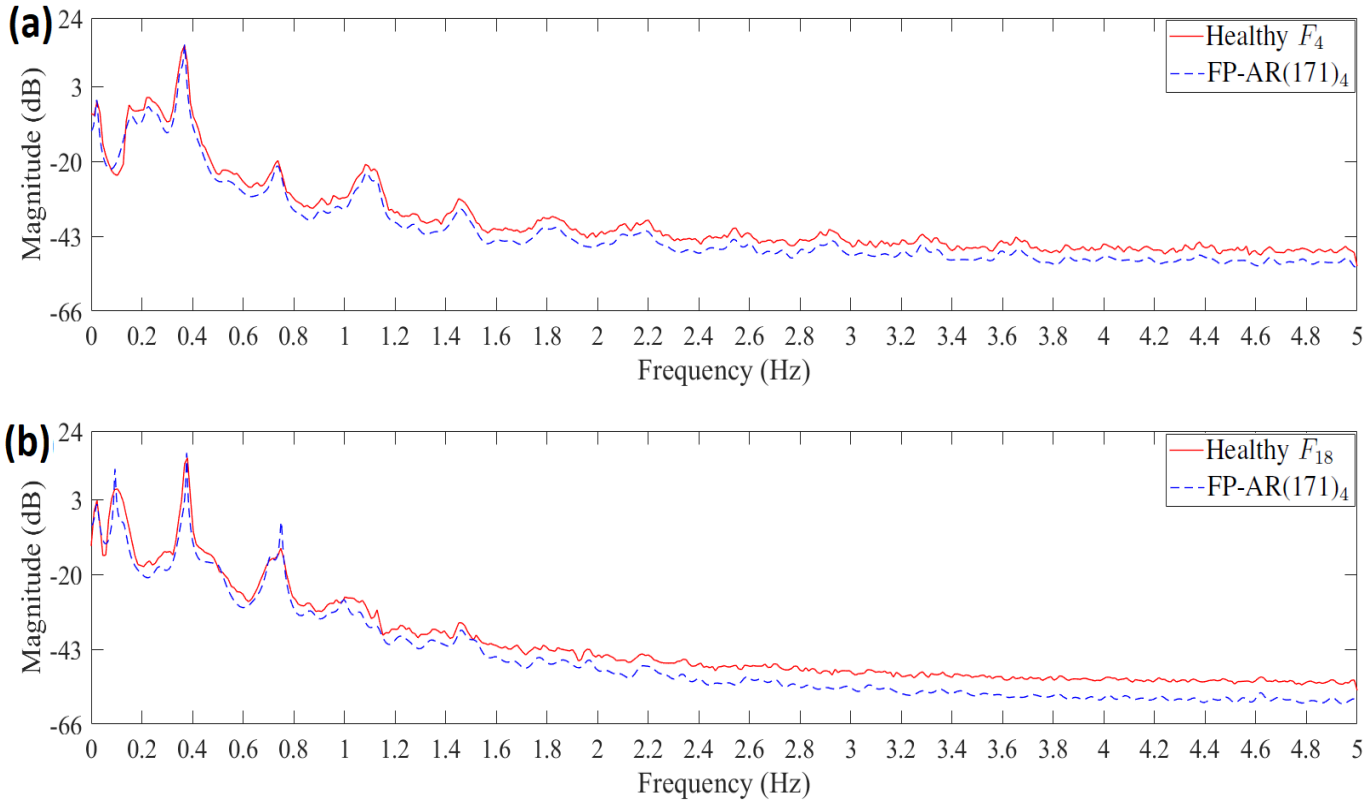

Figure 7. (a) Welch based PSD estimate (——) for the healthy state F_4 and the FP-AR model's PSD estimate (– – –); (b) Welch based PSD estimate (——) for the healthy state F_{18} and the FP-AR model's PSD estimate.

4.2 Inspection phase

Step 1: Damage detection. A response signal corresponding to an unknown structural state is driven through the FP-AR model which is re-parametrized in terms of k (Equation (8)). Then k is estimated based on the NLS estimator of Equation (9) which searches for the estimate $\hat{k}$ leading to the minimum of the estimation criterion. Finally, damage detection is achieved through the corresponding Q statistic based on the normalized autocorrelation of $e_u[t, \hat{k}]$ (Matlab function: *autococorr.m*; see subsection 3.2 and details in Table 3). Thus, it

442 is checked if the model trained to describe healthy dynamics under varying EOCs, is able to describe the current
443 unknown dynamics as well.

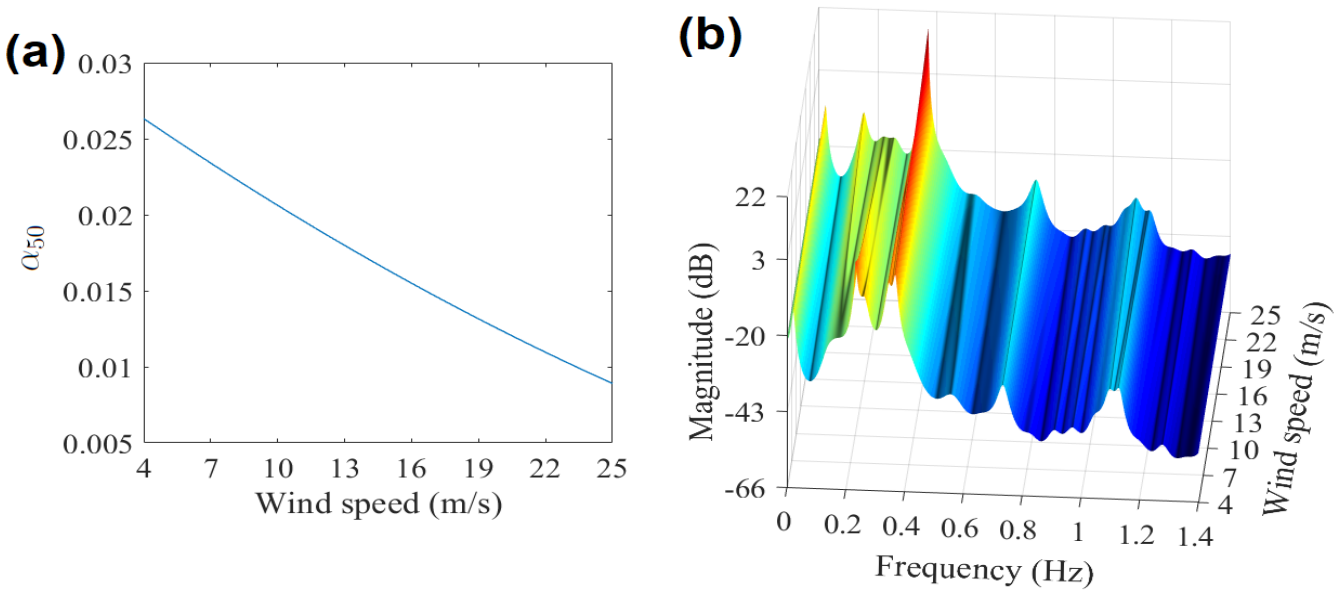

444

445 **Figure 8.** (a) Indicative AR parameter of the FP-AR model as function of WS and (b) PSD magnitude
446 of the FP-AR model as function of frequency and WS.

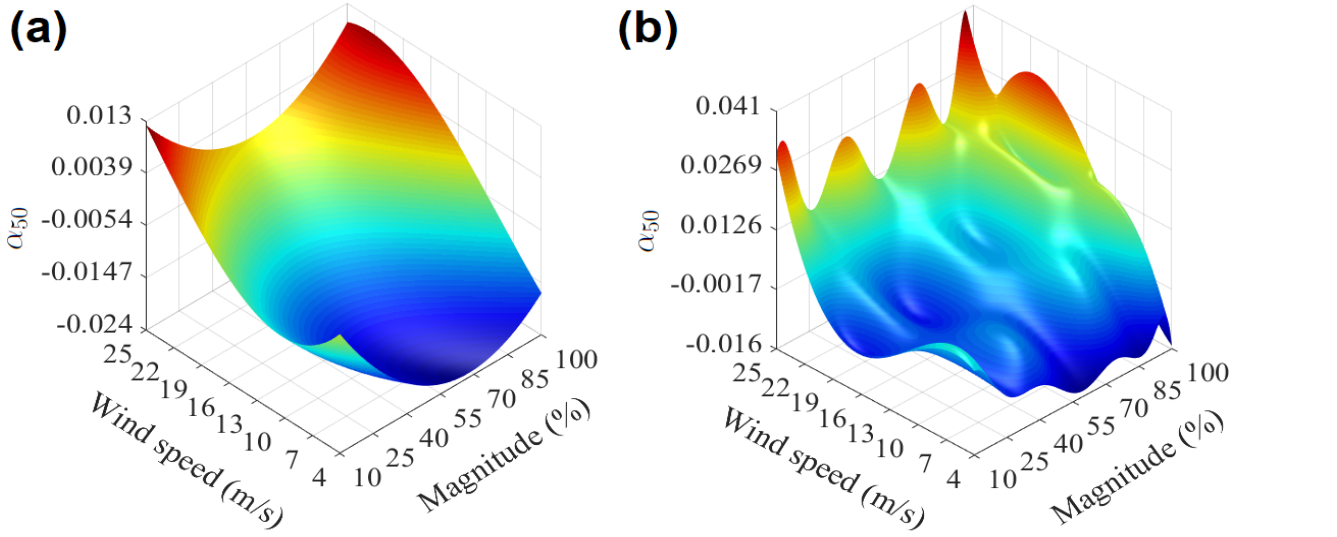

447

448 **Figure 9.** (a) Tendon 6 - VFP-AR model and (b) Tendon 8 - VFP-AR model indicative AR
449 parameter as function of WS and damage magnitude.

450

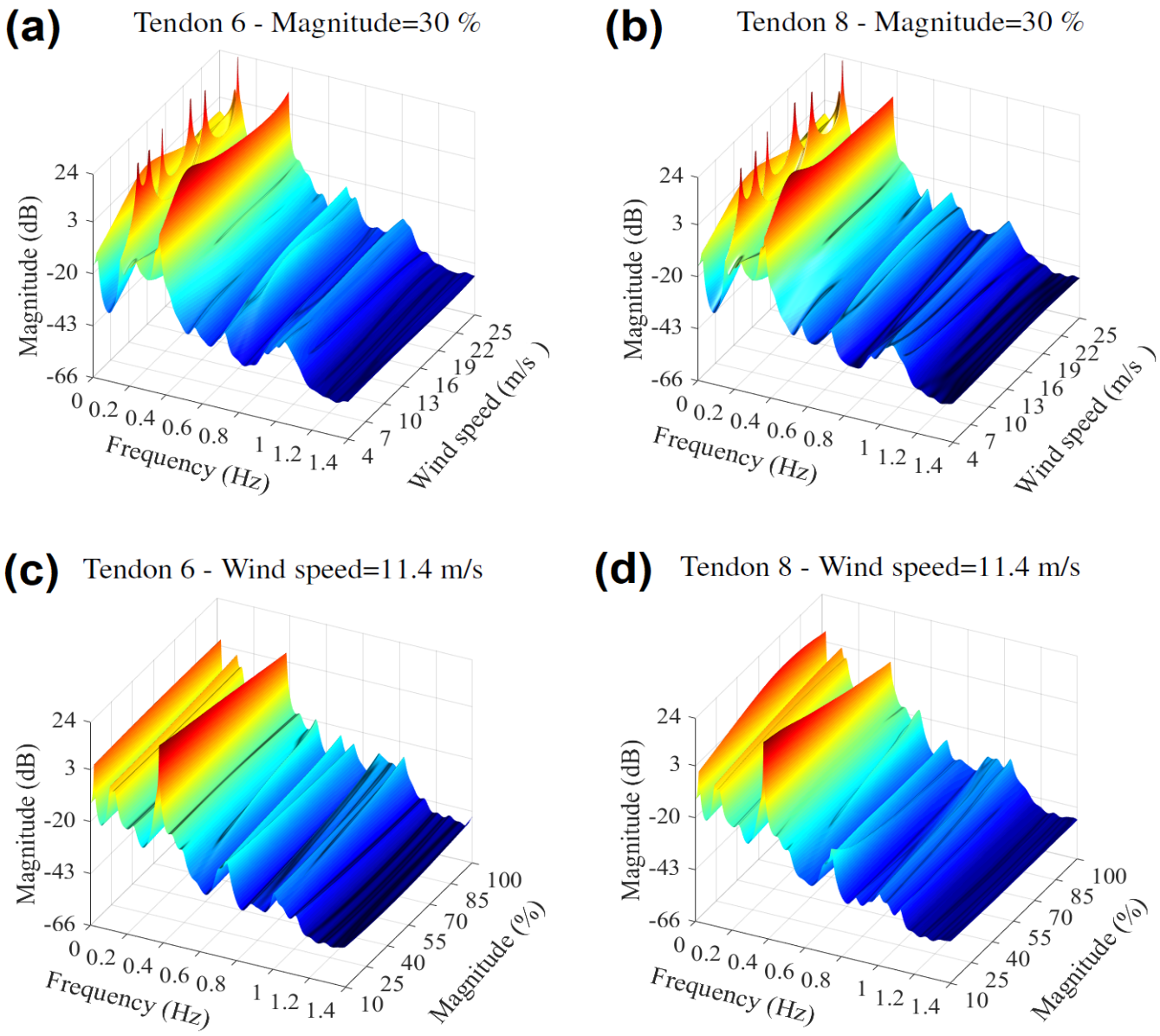

Figure 10. PSD magnitudes of the two VFP-AR models representing the structural dynamics under damaged tendons 6, 8 as function (a),(b) of frequency and WS and (c),(d) of frequency and damage magnitude.

39 healthy and 394 damage cases are examined (see Table 2) with the damage detection results presented through the corresponding Q statistics in Figure 11(a). It must be noted that the Q statistics corresponding to 7 damage cases of magnitude [10-15] % from tendon 8, are not separable from the Q statistics corresponding to healthy cases. This happens due to the effects of the varying EOCs on the healthy FOWT dynamics, fully 'masking' the effects of damages of magnitude [10-15] % (see subsection 2.4).

460 The damage detection results are also presented through a Receiver Operating Characteristic (ROC) curve
461 (Figure 11(b)) and the Area Under the ROC Curve (AUC) (Figure 11(c)). The ROC curve represents the true
462 positive rate (percentage of damages detected correctly) versus the false positive rate (percentage of false alarms)
463 for varying decision threshold, with the perfect detection (no false alarms or missed damages) confirmed when
464 the ROC curve includes the (0,1) point (Matlab function: *perfcurve.m*) [56, 57]. The AUC ranges from 0 to 1
465 with values close to 1 indicating great performance and values close to 0.5 poor performance (Matlab function:
466 *perfcurve.m*) [57]. In Figure 11(b), the ROC curve is very close to the best possible point (0,1) with the true
467 positive rate (correct detection rate) being 98.2 % for false positive rate (false alarm rate) equal to 0 %. The 1.8
468 % missed damages correspond to the aforementioned 7 damages of magnitude [10-15] %. In Figure 11(c), the
469 AUC is 0.9957. The ROC and AUC based results are excellent and they show that damage detection in the
470 tendons of a FOWT under varying EOCs, is almost perfect.

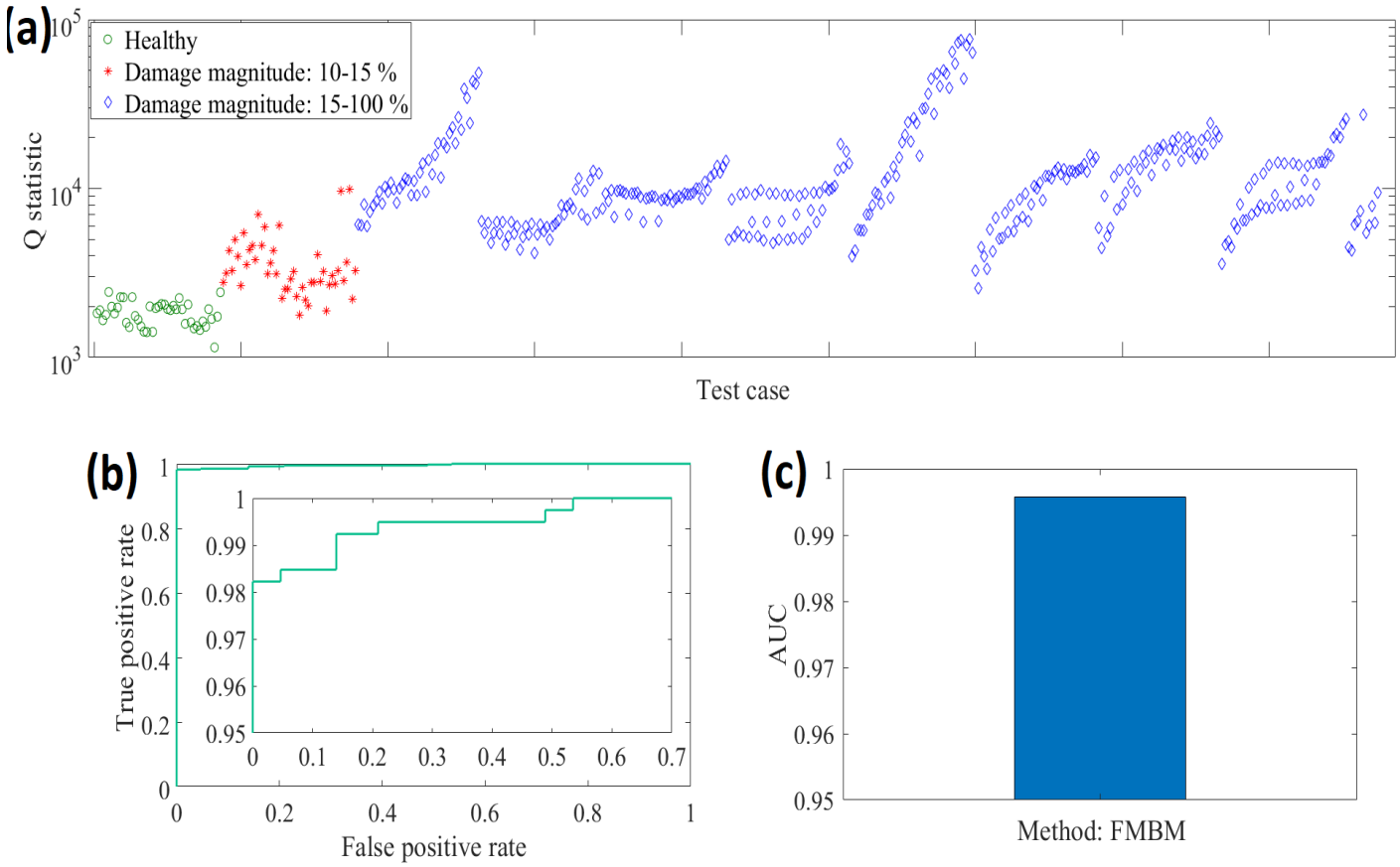

471

472 **Figure 11.** Damage detection performance of the FMBM: (a) the method's Q statistic, (b) the ROC curve and
473 (c) the AUC value (39 healthy and 394 damage cases).

Step 2: Damaged tendon identification. When a damage is detected, damaged tendon identification starts. The response signal corresponding to the unknown detected damage, is driven through each considered baseline VFP-AR model which is re-parametrized in terms of $\boldsymbol{k}$ (Equation (10)). Based on each re-parametrized model, the NLS estimator of Equation (11) obtains the estimate $\widehat{\boldsymbol{k}}$ (see details in Table 3). Then the identification of damaged tendon is achieved through the D statistic based on the partial autocorrelation of $e_u[t, \widehat{\boldsymbol{k}}]$ (Matlab function: *parcocorr.m*; see subsection 3.2 and Table 3).

In Figure 12 (a),(b), estimation of $\boldsymbol{k}$ results are presented for two damage cases from tendons 6, 8. For each damage case, the $\boldsymbol{k}$ estimation is presented based only on the VFP-AR model of the actual tendon. The NLS computes the estimation criterion while searching for the minimum criterion value (criterion values are color coded with the darkest value corresponding to the minimum) on the examined range. Evidently, the actual WS w and magnitude m and their estimates $\widehat{w}$, $\widehat{m}$ are very close, practically coinciding with each other. Moreover, for each damage case, the agreement of the VFP-AR model based PSD with its Welch-based counterpart in Figure 12(c),(d), shows the high accuracy in modelling the damaged structural dynamics under varying EOCs through the selected VFP-AR model.

Due to the fact that the considered damages in this study affect the FOWT dynamics in a highly similar way (see subsection 2.4), damaged tendon identification is achieved through the Portmanteau test by selecting the tendon with the lowest D statistic. Indicative damaged tendon identification results based on damage cases from tendon 6 and 8, are provided in Figure 13 and it is evident that the lowest D statistic leads to the identification of the actual damaged tendon. In this step, the total number of 387 damage cases is considered (the 7 undetected damages are excluded from the 394 damage cases examined in *step 1*), 197 cases from tendon 6 and 190 cases from tendon 8. Damaged tendon identification is achieved successfully in 184 damage cases from tendon 6 with a success rate of 93.4 % and in 188 damage cases from tendon 8 with a success rate of 98.94 %. The no-identification of the actual tendon for the 15 damage cases, happens due to the fact that damages on different tendons similarly affect the platform's structural dynamics (see subsection 2.4). The total success rate 96.12 %

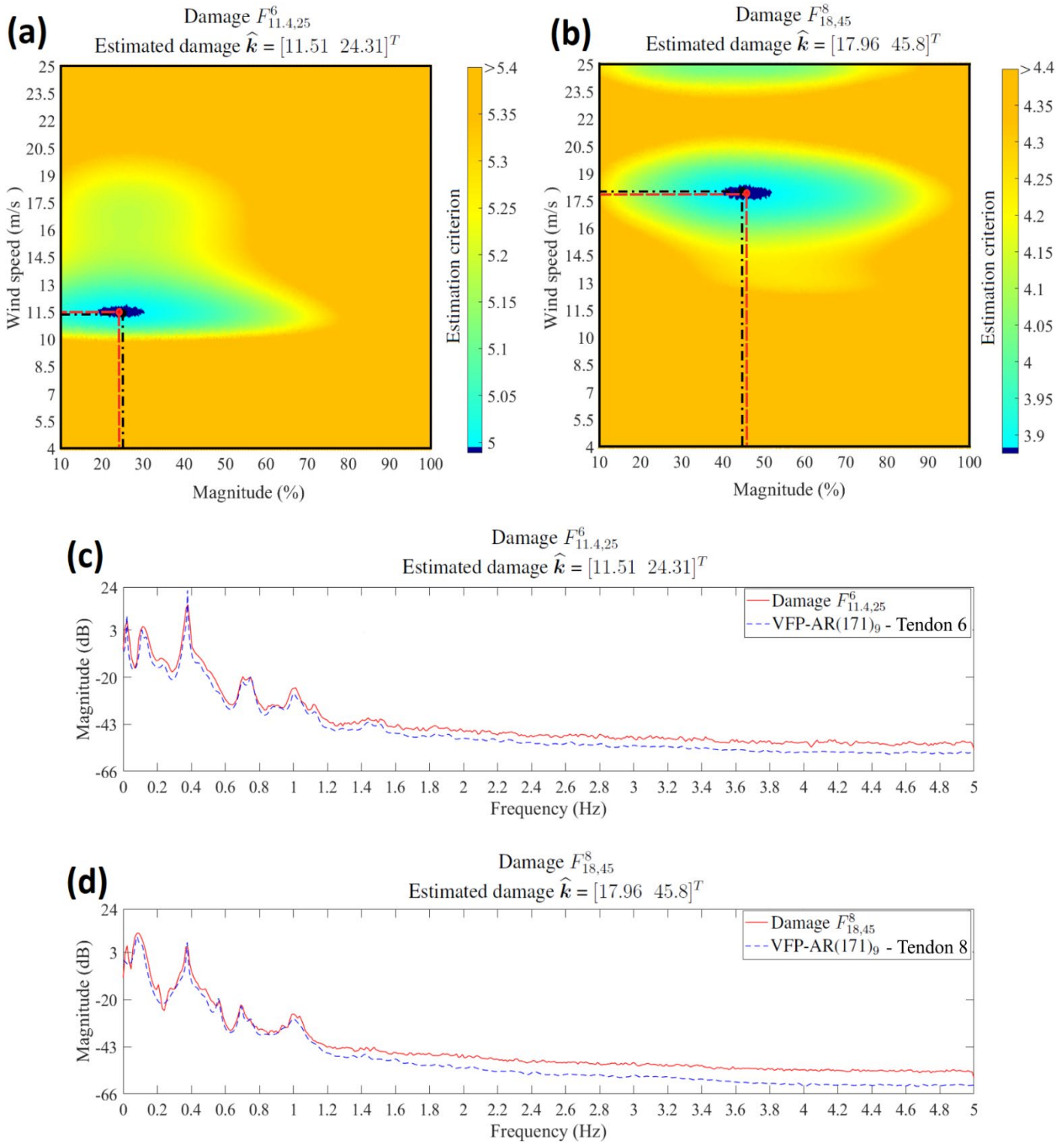

Figure 12. Indicative estimation of $\boldsymbol{k}$ results for two damage cases: (a), (c) $F^6_{11.4,25}$ and (b), (d) $F^8_{18,45}$. (a), (b) The estimation criterion values are shown using a color code (the darkest color indicating minimum, and thus the estimated damage magnitude). The actual WS and damage magnitude (- - -) and theirs estimates (· – · – ·) are also numerically provided over each plot. (c), (d) Welch–based PSD magnitude for the considered WS and damage magnitude (—) compared to that of the VFP-AR model (– –).

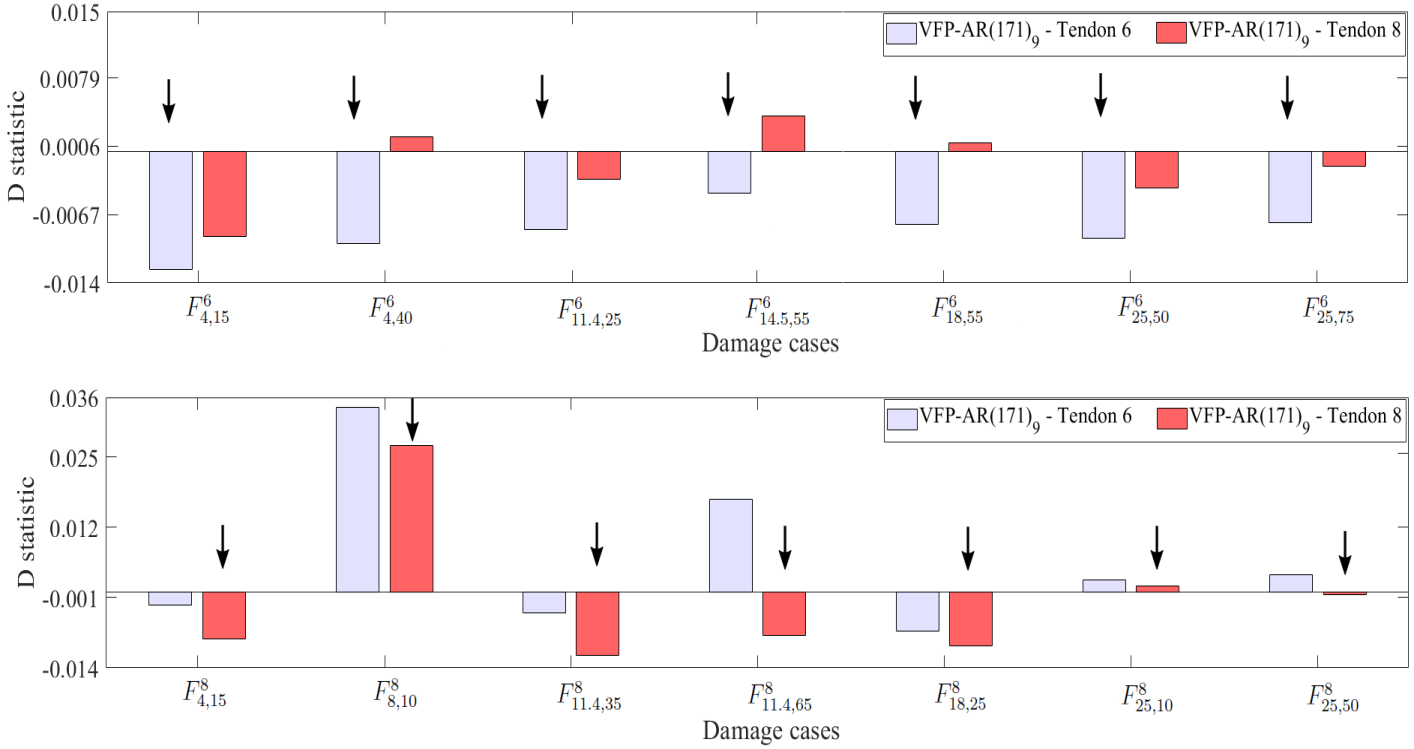

504

505 **Figure 13.** Indicative damaged tendon identification results for 14 damage cases. The actual structural state is
506 presented below each pair of bars. The dark arrow shows the tendon selected as the actual damaged tendon in
507 each case.

508

509 The fact that there are 372 from the 387 damage cases is very high and this shows that damaged tendon
510 identification in a FOWT is achievable in spite of the effects of the varying EOCs and the similarity between
511 the effects of the considered damages. An overview of the corresponding results is provided in Table 4.

512

513 **Table 4.** Damaged tendon identification and damage precise quantification results.

Step 2: Damaged tendon identification			**Step 3: Damage precise quantification**	
Tendon	Model	Identification	Quantification error for wind speed (sample mean ± std)	Quantification error for damage magnitude (sample mean ± std)
6	VFP-AR(171)$_9$	184/197 (93.4 %)	0.19 ± 0.64 (m/s)	4.21 ± 3.02 (%)
8	VFP-AR(171)$_9$	188/190 (98.94 %)	0.17 ± 0.6 (m/s)	4.06 ± 2.90 (%)

514 515 516 517

518

519

520 *Step 3. Damage precise quantification.* After the identification of the damaged tendon, the corresponding
521 estimate $\widehat{\boldsymbol{k}}$ (Equation (11)) is accepted and the confidence intervals are constructed (Equation (12)).

522 Indicative damage precise quantification results in terms of WS and damage magnitude estimates and
523 confidence intervals, are provided in Figure 14. It is obvious that damage precise quantification is achieved at
524 $\alpha = 1 \times 10^{-2}$ as the estimated and the actual WSs and damage quantities are very close, with the actual values
525 being within or just outside of the obtained confidence intervals. A summary of all damage precise
526 quantification results based on the 372 considered damage cases (the 15 unidentified damages are excluded
527 from the 387 damage cases examined in *step 2*), is presented in Table 4 and Figure 15. The quantification error
528 for WS is the error between the actual WS w and its estimate $\widehat{w}$, whereas the quantification error for damage
529 magnitude is the error between the actual damage magnitude m and its estimate $\widehat{m}$. In Figure 15 where the
530 distribution of the quantification error for damage magnitude is presented based on the 372 cases, the error
531 remains smaller than 9 % for 91.31 % of the 184 cases from tendon 6 and for 92.01 % of the 188 cases from
532 tendon 8. The mean quantification errors for magnitude are 4.21 % for tendon 6 and 4.06 % for tendon 8 and
533 the mean errors for WS for tendons 6 and 8 are close to 0 (Table 4). These errors are quite small for large
534 structures such as a FOWT operating under varying EOCs and damages affecting the structural dynamics in a
535 similar manner. They show that damage precise quantification under varying EOCs, can be achieved with a
536 high precision.

537
538

539

540
541

542

543

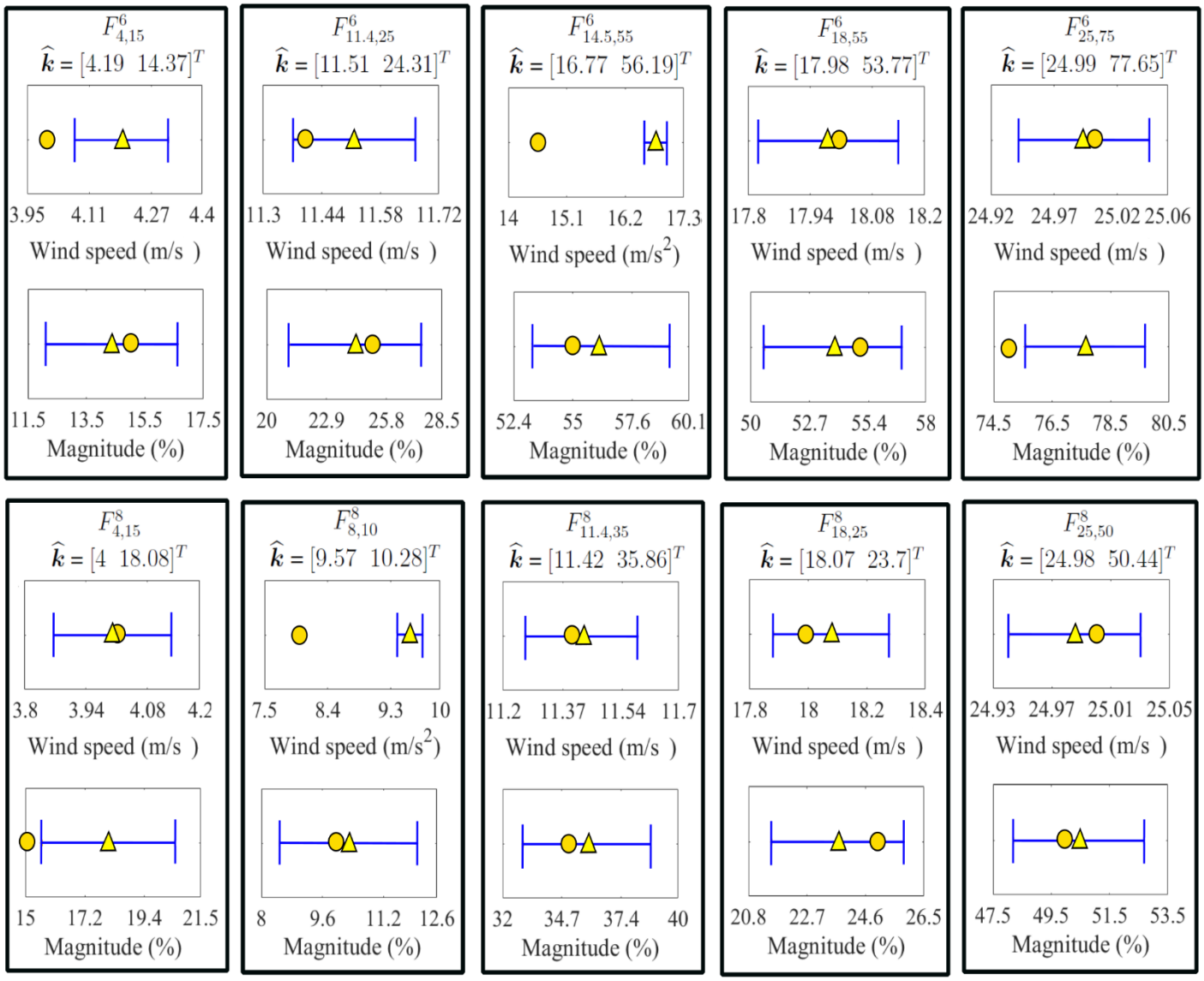

Figure 14. Indicative damage precise quantification results for 10 damage cases (: true WS / damage magnitude; : point estimate; : confidence interval). The true and estimated WS and damage magnitude are numerically provided above each plot.

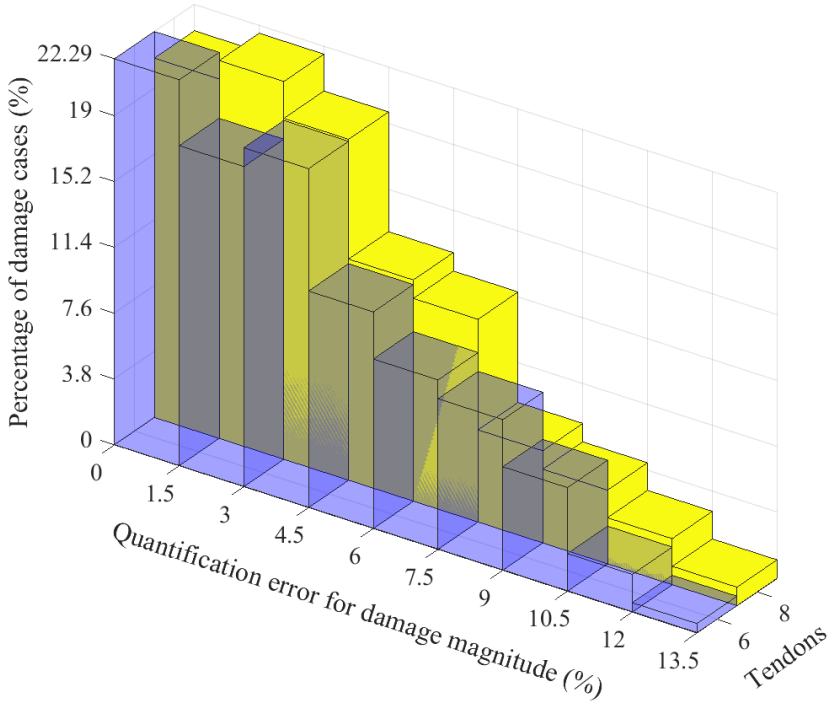

549

550 **Figure 15.** Damage precise quantification results in terms of the quantification error for damage magnitude (%)
551 which is the error between the actual and its estimated damage magnitude (184 damage cases based on tendon
552 6 and 188 damage cases based on tendon 8).

553

554 ## 5. Conclusions

555 The combined problem of damage detection, damaged tendon identification and damage precise
556 quantification in a new type of a FOWT under varying EOCs has been investigated for the first time through
557 the novel FMBM. The method has been formulated to operate using a single response signal from the FOWT
558 received via a single sensor instead of two signals received via two sensors as in the method's previous version.
559 The examined structure is a new concept of FOWT with its tower supported by an improved version of the
560 multibody floating TELWIND platform that consists of two tanks connected via 12 tendons. The FOWT has
561 been subjected to varying EOCs corresponding to seven different WSs and irregular SWHs and current of
562 constant speed and direction, thus reflecting normal and the most severe EOCs of the selected site located in the
563 northern coast of Scotland. The formulated FMBM has been based on FMs where only the WS have been
564 considered as an operating parameter due to the dependence of SWH on WS. Thus, the FMs have represented

565 the structural dynamics under varying EOCs of any potential WS and under any magnitude of the considered
566 damages.

567 Various damage scenarios have been simulated via the stiffness reduction (%) at the tendon's connection
568 point to the upper tank of the platform. Two out of the total 12 tendons have been examined. A numerical
569 coupled model of the FOWT has been used for the simulation of the healthy and damaged structure under
570 varying EOCs. Surge acceleration signals have been collected from the upper tank of the platform, within a
571 limited bandwidth of low frequencies in the range [0-5] Hz corresponding to realistic operating conditions under
572 physical excitation. Furthermore, it is observed that the tendons intersect each other and form an "x-cross"
573 connection. Thus, the caused interference between the crossing tendons is capable of creating wears and it is
574 recommended the effect to be further investigated.

575 The FMBM has been applied under challenging conditions corresponding to i) effects of the varying EOCs
576 on the healthy FOWT, fully "masking" the effects damages of magnitude less than 20 %, ii) small effects of
577 damages of magnitude [20-80] %, on the dynamics due to the high number and robustness of the existing
578 tendons, iii) damages of magnitude [20-80] % on the one tendon under constant WS, having similar effects on
579 the structural dynamics and iv) damages of magnitude [10-100] % on different tendons, having similar effects
580 on the structural dynamics.

581 The main achievements of the study, are presented below:

582 • The modeling of the healthy structural dynamics under varying EOCs of any potential WS in the
583 continuous WS range of [4-25] m/s, has been realized via a single, data-based, response-only, FP-AR
584 model.
585 • More advanced VFP-AR models with an operating parameter vector that includes varying EOCs of any
586 potential WS and damage of any magnitude at a tendon's connection point, have been employed for the
587 representation of the structural dynamics under damage and varying EOCs.

- Damage detection has been remarkable with correct detection for 98.2 % of the considered damage cases (394) and zero false alarms achieved. This achievement has happened in spite of the subtle nature of the considered damages causing slight changes on the structural dynamics and the effects of EOCs on the dynamics being confused with the effects of the damages.
- Damaged tendon identification, that is the determination of the specific tendon that is damaged, has been achieved for 96.12 % of the damage cases (387). This has been, independent from the fact that there has been great similarity in the effects caused to the structural dynamics by the considered damages on the different tendons and the difficulty added by the varying EOCs.
- The mean error in damage precise quantification has been approximately 4% in terms of tendon stiffness reduction for both tendons and all considered cases (372). The obtained damage magnitude confidence intervals have included in most cases (or they are too close) the actual damage magnitude. Based on this along with the previously mentioned difficulties of the subtle damages and the varying EOCs, the obtained damage precise quantification results have been judged as very good.
- This study has confirmed that advanced stochastic methods such as the FMBM can successfully perform SHM under varying EOCs and achieve complete diagnosis of damages in FOWTs' tendons, using limited (even a single) vibration measurements.

Acknowledgements

This project is funded by European Regional Development Fund (ERDF), Interreg Atlantic Area (grant number: EAPA_344/2016) and the European Union's Horizon 2020 research and innovation programme under the Marie Skłodowska-Curie grant agreement no. 730888 (RESET).

References

[1] C.P. Fritzen, M. Klinkov, P. Kraemer, Vibration-based damage diagnosis and monitoring of external loads, in: W. Ostachowicz, J.A. Güemes (Eds.), New Trends in Structural Health Monitoring. 542 of International Centre for Mechanical Sciences Courses and Lectures, Springer, Vienna, 2013.

[2] G. Oliveira, F. Magalhães, Á. Cunha, E. Caetano, Vibration-based damage detection in a wind turbine using 1 year of data, Structural Control Health Monitoring 25 (11) (2018) e2238.

[3] M. Martinez-Luengo, A. Kolios, L. Wang, Structural health monitoring of offshore wind turbines: A review through the Statistical Pattern Recognition Paradigm, Renewable and Sustainable Energy Reviews 64 (2016) 91-105.

[4] H. Sohn, Effects of environmental and operational variability on structural health monitoring, Philosophical Transactions of the Royal Society A: Mathematical, Physical and Engineering Sciences. 365 (1851) (2007) 539-560.

[5] M.M. Ettefagh, Damage identification of a TLP floating wind turbine by meta-heuristic algorithms, Chinese Ocean Engineering 29 (6) (2015) 891-902.

[6] V. Jahangiri, H. Mirab, R. Fathi, M.M. Ettefagh, TLP structural health monitoring based on vibration signal of energy harvesting system, Latin American Journal of Solids and Structures 13 (5) (2016) 897-915.

[7] S. Chandrasekaran, T. Chithambaram, Health monitoring of tension leg platform using wireless sensor networking: experimental investigations, Journal of Marine Science and Technology 24 (2019) 60-72.

[8] C.S. Sakaris, M. Bashir, Y. Yang, C. Michailides, J. Wang, J.S. Sakellariou, Diagnosis of damaged tendons on a 10 MW multibody floating offshore, wind turbine platform via a response-only functional model based method, Engineering Structures 242 (2021) 112384.

[9] S. Chandrasekaran, T. Chithambaram, Structural health monitoring of offshore buoyant leg storage and regasification platform: Experimental investigations, Journal of Marine Science and Applications 17 (2018) 87-100.

[10] A. Jamalkia, M.M. Ettefagh, A. Mojtahedi, Damage detection of TLP and Spar floating wind turbine using dynamic response of the structure, Ocean Engineering 125 (2016) 191-202.

[11] S.E. Begg, N. Fowkes, T. Stemler, L. Cheng, Fault detection in vibration systems: Identifying damaged moorings, Ocean Engineering 164 (2018) 2018577-589.

[12] P. Wang, X. Tian, T. Peng, Y. Luo, A review of the state-of-the-art developments in the field monitoring of offshore structures, Ocean Engineering 147 (2018) 148-164.

[13] D. Tang, J. Chen, W. Wu, L. Jin, Q. Yu, Bin Xie, S. Wang, J. Feng, Research on sampling rate selection of sensors in offshore platform shm based on vibration, Applied Ocean Research 101 (2020) 102192.

[14] A.A. Elshafey, M.R. Haddara, H. Marzouk, Damage detection in offshore structures using neural networks, Marine Structures 23 (2010) 131-145.

[15] A. Mojtahedi, M.A. Lotfollahi Yaghin, Y. Hassanzadeh, M.M. Ettefagh, M.H. Aminfar, A.B.Aghdam, Developing a robust SHM method for offshore jacket platform using model updating and fuzzy logic system, Applied Ocean Research 33 (4) (2011) 398-411.

[16] F. Liu, H. Li, W. Li, B. Wang, Experimental study of improved modal strain energy method for damage localisation in jacket-type offshore wind turbines, Renewable Energy 72 (2014) 174-181.

[17] S. Jeong, E.J. Kim, D.H. Shin, J.W. Park, S.H. Sim, Data fusion-based damage identification for a monopile offshore wind turbine structure using wireless smart sensors, Ocean Engineering 195 (2020) 106728.

[18] M.M. Luczak, J. Telega, N. Zagato, E. Mucchi, On the damage detection of a laboratory scale model of a tripod supporting structure by vibration-based methods, Marine Structures 64 (2019) 146-160.

[19] M. Mieloszyk, W. Ostachowicz, An application of Structural Health Monitoring system based on FBG sensors to offshore wind turbine support structure model, Marine Structures 51 (2017) 65-86.

[20] R. Soman, Semi-automated methodology for damage assessment of a scaled wind turbine tripod using enhanced empirical mode decomposition and statistical analysis, International Journal of Fatigue 134 (2020) 105475.

[21] M.L. Wymore, J.E. Van Dam, H. Ceylan, D. Qiao, A survey of health monitoring systems for wind turbines, Renewable and Sustainable Energy Reviews 52 (2015) 976-990.

[22] B. Qiu, Y. Lu, L. Sun, X. Qu, Y. Xue, F. Tong, Research on the damage prediction method of offshore wind turbine tower structure based on improved neural network, Measurement 151 (2020) 107141.

[23] H.C. Kim, M.H. Kim, D.E. Choe, Structural health monitoring of towers and blades for floating offshore wind turbines using operational modal analysis and modal properties with numerical-sensor signals, Ocean Engineering 188 (2019) 106226.

[24] W. Weijtjens, T. Verbelen, G.D. Sitter, C. Devriendt, Foundation structural health monitoring of an offshore wind turbine-a full-scale case study, Structural Health Monitoring 15 (4) (2016) 389-402.

[25] P. Kraemer, H. Friedmann, C. Ebert, J. Mahowald, B. Wölfel, Experimental validation of stochastic subspace algorithms for structural health monitoring of offshore wind turbine towers and foundations, Proceedings of the 8th European Workshop on Structural Health Monitoring (EWSHM), Bilbao, Spain, 2016.

[26] A. Rytter, Vibration based inspection of civil engineering structures, PhD thesis, Department of Building Technology and Structural Engineering, Aalborg University, Denmark, 1993.

[27] T.C.I. Aravanis, J.S. Sakellariou, S.D. Fassois, A stochastic Functional Model based method for random vibration based robust fault detection under variable non–measurable operating conditions with application to railway vehicle suspensions, Journal of Sound and Vibration 466 (2020) 115006.

[28] T.C.I. Aravanis, J.S. Sakellariou, S.D. Fassois, On the Functional Model based method for vibration-based robust damage detection: versions and experimental assessment, Structural Health Monitoring (2020).

[29] J.S. Sakellariou, S.D. Fassois, C.S. Sakaris, Vibration-based damage localization and estimation via the stochastic Functional Model Based Method (FMBM) - an overview, Structural Health Monitoring 17 (6) (2018) 1335-1348.

[30] A.G. Poulimenos, J.S. Sakellariou, A transmittance-based methodology for damage detection under uncertainty: An application to a set of composite beams with manufacturing variability subject to impact damage and varying operating conditions, Structural Health Monitoring 18 (1) (2019) 318-333.

[31] F.P. Kopsaftopoulos, S.D. Fassois, A functional model based statistical time series method for vibration based damage detection, localization, and magnitude estimation, Mechanical Systems and Signal Processing 39 (1-2) (2013) 143-161.

[32] C.S. Sakaris, J.S. Sakellariou, S.D. Fassois, Vibration-based damage precise localization in three-dimensional structures: Single versus multiple response measurements, Structural Health Monitoring 14 (3) (2015) 300-314.

[33] C.S. Sakaris, J.S. Sakellariou, S.D. Fassois, A time series generalized functional model based method for vibration-based damage precise localization in structures consisting of 1D, 2D and 3D elements, Mechanical Systems and Signal Processing 74 (2016) 199-213.

[34] C.S. Sakaris, J.S. Sakellariou, S.D. Fassois, Random-vibration-based damage detection and precise localization on a lab-scale aircraft stabilizer structure via the Generalized Functional Model Based Method, Structural Health Monitoring 16 (5) (2017) 594-610.

[35] C.S. Sakaris, J.S. Sakellariou, S.D. Fassois, Vibration-based multi-site damage precise localization via the Functional Model Based Method, Procedia Engineering 199 (2017) 2072-2077.

[36] C.S. Sakaris, Random vibration based precise localization of single and multi-site structural damage via stochastic Functional Models, Ph.D. thesis, Department of Mechanical Engineering and Aeronautics, University of Patras, Greece, 2018.

[37] J.S. Sakellariou, S.D. Fassois, Vibration based fault detection and identification in an aircraft skeleton structure via a stochastic functional model based method, Mechanical Systems and Signal Processing, 22 (3) (2008) 557-573.

[38] J.S., Sakellariou, K.A., Petsounis, S.D., Fassois, Vibration based fault diagnosis for railway vehicle suspensions via a functional model based method: A feasibility study, Journal of Mechanical Science and Technology volume 29 (2015) 471–484.

[39] Y. Yang, M. Bashir, J. Wang, C. Michailides, S. Loughney, S. Hernandez, J. Urbano, M. Armin, L. Chun, Wind-wave coupling effects on the fatigue damage of tendons for a 10 MW multi-body floating wind turbine, Ocean Engineering 217 (2020) 107909.

[40] J.A. Armesto, A. Jurado, R. Guanche, B. Couñago, J. Urbano, J. Serna, TELWIND: Numerical Analysis of a Floating Wind Turbine Supported by a Two Bodies Platform. Proceedings of the 37th International Conference on Ocean, Offshore and Arctic Engineering (OMAE), Madrid, Spain, 2018, V010T09A073.

[41] J.M. Jonkman, L. Kilcher, TurbSim User's Guide: Version 1.06.00. National Renewable Energy Laboratory, U.S. Department of Energy Office of Energy Efficiency & Renewable Energy, Report no. NREL/TP-xxx-xxxx, 2012, p. 30.

[42] J.M.J. Journee, W.W. Massie, Offshore hydromechanics, 1st ed. Delft University of Technology, Delft, 2001, pp. 40-41.

[43] S.K. Chakrabarti, Handbook of offshore engineering, 1st ed. Elsevier, London, 2005, pp. 106-108.

[44] Y. Yang, M. Bashir, C. Michailides, J. Wang, Development and application of an aero-hydro-servo-elastic coupling framework for analysis of floating offshore wind turbines, Renewable Energy 261 (2020) 606-625.

[45] J.M. Jonkman, M.L.J. Buhl, FAST user’s guide, National Renewable Energy Laboratory, U.S. Department of Energy Office of Energy Efficiency & Renewable Energy, Report no. NREL/TP-500-38230, 2005.

[46] Y. Yang, M. Bashir, C. Michailides, X. Mei, J. Wang, L. Chun. Coupled analysis of a 10 MW multi-body floating offshore wind turbine subjected to tendon failures. Renewable Energy 176 (2021) 89-105.

[47] P. Stoica, R. Moses, Introduction to spectral analysis, Prentice-Hall, New Jersey, 1997, pp. 52-53.

[48] L. Ljung, System identification: Theory for the user, 2nd ed. Prentice Hall, New Jersey, 1999.

[49] R.L. Haupt, S.E. Haupt, Practical genetic algorithms, 2nd ed. John Wiley & Sons, New Jersey, 2004, pp. 27-49.

[50] J.S. Sakellariou, S.D. Fassois, Functionally Pooled models for the global identification of stochastic systems under different pseudo-static operating conditions, Mechanical Systems and Signal Processing 72-73 (2016) 785-807.

[51] D. Peña, J. Rodríguez, The log of the determinant of the autocorrelation matrix for testing goodness of fit in time series, Journal of Statistical Planning and Inference 136 (8) (2006) 2706-2718.

[52] G.E.P. Box, G.M. Jenkins, G.C. Reinsel, Time series analysis: Forecasting and control, 3rd ed. Prentice-Hall, New Jersey, 1994.

[53] F. Kopsaftopoulos, R. Nardari, Y.H. Li, F.K. Chang, A stochastic global identification framework for aerospace structures operating under varying flight states, Mechanical Systems and Signal Processing 98 (2018) 425-447.

[54] G.E. Forsythe, M.A. Malcolm, C.B. Moler, Computer methods for mathematical computations. Prentice-Hall, New Jersey, 1976, pp. 178-184.

[55] J. Nocedal, S.J. Wright, Numerical Optimization, 2nd ed. Springer, New York, 2006, pp. 529-561.

[56] R. Duda, P. Hart, D. Stork, Pattern classification, 2nd ed. Wiley, 2000, pp. 34-35.

[57] T. Fawcett, An introduction to ROC analysis, Pattern Recognition Letters 27 (8) (2006) 861-874.